Charge transport in charge-ordered layered crystals θ-(BEDT-TTF)$_2M$Zn(SCN)$_4$ (M=Cs,Rb): Effects of long-range Coulomb interaction and the Pauli exclusion principle

Yamaguchi Takahide,[1] Motoi Kimata,[1] Kaori Hazama,[1,2] Taichi Terashima,[1] Shinya Uji,[1,2] Takako Konoike,[3] and Hiroshi M. Yamamoto[4]

[1]*National Institute for Materials Science, Tsukuba 305-0047, Japan*

[2]*University of Tsukuba, 1-1-1 Tennodai, Tsukuba 305-8571, Japan*

[3]*Institute for Solid State Physics, The University of Tokyo, Kashiwa 277-8581, Japan*

[4]*RIKEN (The Institute of Physical and Chemical Research), Wako 351-0198, Japan*

(Received 14 October 2009; revised manuscript received 10 March 2010; published 11 June 2010)

We have measured the current-voltage (I-V) characteristics, dielectric properties, and magnetoresistances of insulating layered organic crystals θ-(BEDT-TTF)$_2M$Zn(SCN)$_4$ (M=Cs,Rb), in which electron-electron Coulomb interactions are considered to induce charge ordering. The in-plane I-V characteristics follow the power law with a large exponent that exceeds 10 in the low-temperature limit. The nonlinear I-V characteristics are attributed to electric field induced unbinding of pairs of an electron and a hole that are thermally excited and attracted to each other due to two-dimensional long-range Coulomb interaction. The temperature and frequency dependences of the in-plane dielectric constant for M=Cs are explained by the polarization of the electron-hole bound pairs, consistently with the I-V characteristics. The large dielectric anisotropy ($\approx$100 at 0.6 K) observed for M=Cs suggests two-dimensional long-range Coulomb interaction, which is also consistent with the explanation of the nonlinear I-V curves. The organic crystals have a large positive magnetoresistance ratio, e.g., $\approx$10 000% for M=Cs in a magnetic field of 10 T at 0.1 K. The magnetoresistance is nearly independent of the magnetic field orientation despite the highly two-dimensional charge transport, indicating that it is electron-spin related. The magnetoresistance may be caused by magnetic field induced parallel alignment of spins of mobile and localized electrons, both in the highest occupied molecular orbital of a BEDT-TTF molecule, and by the resulting suppression of conduction due to the Pauli exclusion principle.

DOI: 10.1103/PhysRevB.81.235110 PACS number(s): 72.20.Ht, 72.80.Le, 75.47.−m, 77.84.Jd

I. INTRODUCTION

Layered organic crystals (BEDT-TTF)$_2X$, consisting of organic molecules BEDT-TTF [bis(ethylenedithio)tetrathiafulvalene] and X=I$_3$, CsZn(SCN)$_4$, etc., are quasi-two-dimensional systems that exhibit various interesting phases such as superconductivity,[1,2] spin liquids,[3] graphenelike zero-gap semiconductivity,[4] and charge ordering.[5] Layers of BEDT-TTF and layers of X are stacked alternately in the crystal [Fig. 1(a)]. The X layers are insulating because X becomes a closed-shell anion X^- by accepting an electron from the BEDT-TTF layer. Transfer integrals on the order of 0.1 eV between the highest occupied molecular orbitals (HOMOs) of neighboring BEDT-TTF molecules lead to a two-dimensional (2D) energy band. Because of the transfer of electrons from the BEDT-TTF layer to the X layer, this band is 3/4 filled; therefore, the crystals are expected to be metallic. For example, θ-(BEDT-TTF)$_2$I$_3$ is actually metallic (superconducting with T_C=3.6 K), exhibiting de Haas–van Alphen oscillations consistent with the Fermi surface calculated from the tight-binding model.[8] However, many of the (BEDT-TTF)$_2X$ family are insulating, which has been considered to be due to electron-electron Coulomb repulsion.

The salt κ-(BEDT-TTF)$_2$Cu[N(CN)$_2$]Cl has been interpreted as a Mott insulator due to on-site Coulomb repulsion.[9,10] The BEDT-TTF molecules dimerize in this salt, leading to an effective half-filled band, which is a base of Mott insulators. The salts θ-(BEDT-TTF)$_2M$Zn(SCN)$_4$ (M=Cs, Rb) also show insulating behavior at low temperatures.[6] There is some evidence that charge ordering with spatially modulated charge distributions occurs in these salts. In the θ-(BEDT-TTF)$_2X$ family, the dihedral angle between BEDT-TTF molecules [see Fig. 1(b)] and hence the transfer integral depends on the kind of anion X^-. The nearest-neighbor transfer integral of θ-(BEDT-TTF)$_2$CsZn(SCN)$_4$ (CsZn salt) is larger than that of θ-(BEDT-TTF)$_2$RbZn(SCN)$_4$ (RbZn salt). Therefore, although both are insulating, the CsZn salt is closer to the metallic phase than the RbZn salt[6] [Fig. 1(c)].

The nonlinear I-V characteristics of the CsZn salt were first reported by Inagaki *et al.*[11] They observed that the in-plane conductivity at 4.2 K increased by 2 orders of magnitude when the electric field was increased up to 6 V/cm. On the basis of an experimental finding that the intensity of x-ray diffuse scattering corresponding to charge modulation along the c axis decreases with increasing current, they attributed the nonlinearity to current-induced melting of insulating charge-order domains.[12–15] However, no quantitative explanation of the nonlinear I-V curves has yet been given. In addition, they measured the I-V curves in a relatively high current region (10^{-7}–10^{-2} A), which is disadvantageous in terms of self-heating. The nonlinear I-V characteristics of the CsZn salt under uniaxial strain have also been reported.[16]

In this study, we have measured the I-V characteristics of θ-(BEDT-TTF)$_2M$Zn(SCN)$_4$ (M=Cs, Rb) in a low current region (10^{-13}–10^{-8} A) at low temperatures (0.1–60 K) to clarify the mechanism responsible for nonlinear I-V curves. The I-V characteristics we obtained can be explained with a simple model assuming a long-range Coulomb interaction, especially one that is logarithmic in distance. We expect that

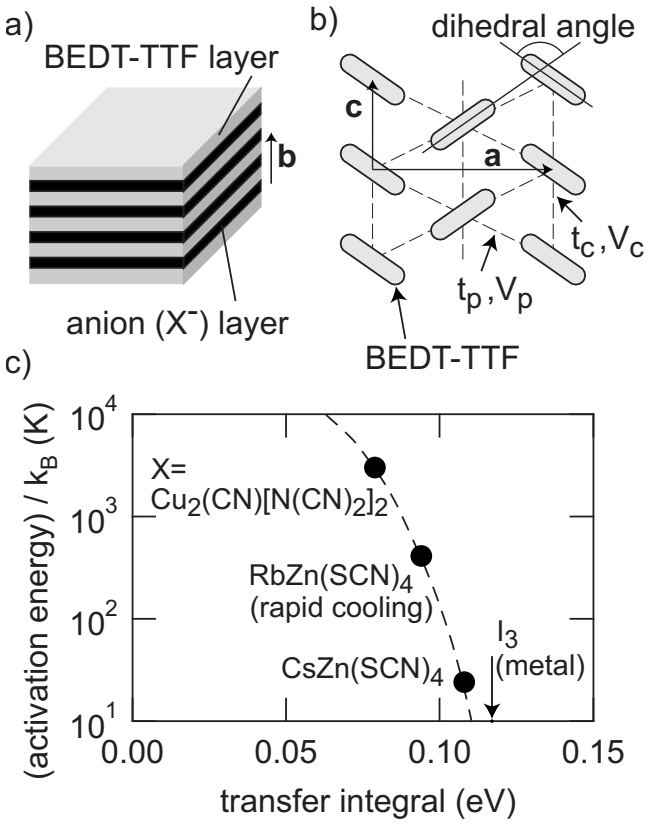

FIG. 1. (a) Schematic of the layered organic crystal θ-(BEDT-TTF)$_2X$[X=CsZn(SCN)$_4$,RbZn(SCN)$_4$]. (b) Arrangement of BEDT-TTF molecules in the BEDT-TTF layer of θ-(BEDT-TTF)$_2M$Zn(SCN)$_4$ (M=Cs, Rb). (c) Activation energy of θ-(BEDT-TTF)$_2X$ plotted as a function of transfer integral [=(bandwidth)/8] (Ref. 6). We obtained the activation energy of θ-(BEDT-TTF)$_2$Cu$_2$(CN)[N(CN)$_2$]$_2$ from the lowest-temperature part of the temperature dependence of conductivity in Ref. 7. The dashed line is a guide to the eye.

this mechanism for nonlinear I-V curves is common in layered organic crystals whose insulating properties are caused by electron-electron Coulomb interactions. We actually found that the Mott insulator κ-(BEDT-TTF)$_2$Cu[N(CN)$_2$]Cl exhibits nonlinear I-V curves similar to those of θ-(BEDT-TTF)$_2M$Zn(SCN)$_4$ (M=Cs, Rb).[17] The logarithmic interaction can be understood if we assume large anisotropy in the dielectric constant. We measured the dielectric constant of θ-(BEDT-TTF)$_2$CsZn(SCN)$_4$ in both the in-plane and out-of-plane directions at 1–100 kHz, and observed large anisotropy $\approx$100 in the low-temperature limit (0.6 K).

We have also observed a large positive magnetoresistance ratio in θ-(BEDT-TTF)$_2M$Zn(SCN)$_4$ (M=Cs, Rb). Despite the highly nonlinear I-V characteristics, the magnetoconductance ratio is independent of the applied voltage. The magnetoconductance curve has little dependence on the direction of the magnetic field, indicating that it is electron-spin related. Furthermore, the magnetoconductance ratio is described by a simple function of $\mu_B B/k_B T$, where μ_B is the Bohr magneton. We suggest that the magnetoconductance is caused by magnetic field induced parallel alignment of spins of mobile and localized electrons, both in the HOMO of the BEDT-TTF molecule, and by the resulting suppression of electrical conduction due to the Pauli exclusion principle.

This paper is organized as follows. Section II briefly reviews previous experimental results on θ-(BEDT-TTF)$_2M$Zn(SCN)$_4$ (M=Cs, Rb) and related theories. We describe experimental methods in Sec. III. In the sections that follow, we describe the experimental results on the dependence of low-bias resistance on temperature (Sec. IV), current-voltage characteristics (Sec. V), dielectric properties (Sec. VII), and magnetoconductance (Sec. VIII). Section VI presents a simple model that we use to explain the nonlinear I-V curves. The estimate of self-heating effects is presented in Sec. IX. Finally, we conclude in Sec. X.

II. PREVIOUS EXPERIMENTAL RESULTS AND THEORIES

This section briefly reviews previous experimental results on θ-(BEDT$-$TTF)$_2M$Zn(SCN)$_4$ (M=Cs, Rb) and related theories.

A. Slowly cooled θ-(BEDT-TTF)$_2$RbZn(SCN)$_4$

The resistivity of the RbZn salt rapidly increases at $\approx$200 K when the sample is slowly cooled typically at a rate of $<$1 K/min.[6,18] This resistive transition accompanies doubling of the unit cell along the c axis.[18–20] Note that in the CsZn and RbZn salts the a and c axes are parallel to the BEDT-TTF layers (in-plane) and the b axis is perpendicular to them (out-of-plane); see Figs. 1(a) and 1(b). The ^{13}C-NMR,[21] polarized Raman, and infrared spectra[22–24] are consistent with an occurrence of a charge disproportionation with the "horizontal stripe" (charge modulation along the c axis) at $20 \leq T \leq 190$ K suggested by the x-ray diffraction data. The charge disproportionation ratio has been estimated to be (0–0.2):(0.8–1.0) from several different data: the ^{13}C-NMR spectra (at $20 \leq T \leq 190$ K),[5,21] the Raman spectra (at T=50 K),[24] and bond lengths in the inequivalent BEDT-TTF molecules (at T=90 K).[20]

The spin susceptibility of the slowly cooled RbZn salt has a broad maximum around 170 K, and it can be fitted to the one-dimensional Heisenberg model with $J=-157$ K at $50 < T < 190$ K.[6] At lower temperatures ($\leq$20 K), the spin susceptibility decreases rapidly with decreasing temperature, indicating the formation of spin singlets. The relaxation rate T_1^{-1} of ^{13}C NMR decreases rapidly below 20 K, consistent with the formation of spin singlets.[5,25] X-ray diffraction measurements suggest dimerization of the hole-rich BEDT-TTF molecules in chains along the a axis.[26] Thus, these results indicate a spin-Peierls transition at $T \approx 20$ K; namely, the electron singly occupying the HOMO in the hole-rich BEDT-TTF molecules forms a spin singlet with its nearest neighbor. Note that the spin susceptibility increases at $T \leq 10$ K,[6,25] indicating that small numbers of paramagnetic spins remain at such low temperatures.

Another feature of the slowly cooled RbZn salt is that diffuse rods of $q=(1/3,k,1/4)$ were observed in the x-ray measurements at $T > 200$ K.[19,20] In this temperature region, the ^{13}C-NMR spectrum broadens,[5,27] which is attributed to

charge disproportionation with slow fluctuations.[27] The diffuse rods disappear at $T<200$ K when the salt is cooled slowly.[19,20]

B. Rapidly cooled θ-(BEDT-TTF)$_2$RbZn(SCN)$_4$

When the RbZn salt is cooled rapidly at a typical rate of ≥ 5 K/min, the resistivity increases gradually without demonstrating the sharp increase at ≈ 200 K observed for slow-cooling. The diffuse rods at $q=(1/3,k,1/4)$ seen at $T>200$ K weaken but still exist at 90 K. Diffuse rods at $q=(0,k,1/2)$ are also observed at 90 K.[19] Thus, two kinds of short-range charge orders with $q=(0,k,1/2)$ and $(1/3,k,1/4)$ seem to coexist at $T<200$ K. A C=C stretching mode in the Raman spectra, although broad, appears at a frequency close to that at the charge-rich site of the slowly cooled RbZn salt.[28] This indicates that a short-range charge order that has a large amplitude occurs in the rapidly cooled RbZn salt. However, ^{13}C-NMR spectra are broad and do not split into two sets of peaks as they do in the slow-cooling case.[29] Kanoda *et al.*[29] suggested the possibility of glassy charge disproportionation. The spin susceptibility increases with decreasing temperature at $T<90$ K, at which the ^{1}H-NMR spin-lattice relaxation rate, T_1^{-1}, is enhanced.[25] Nakamura *et al.*[25] suggested that spin singlets are formed in most sites but some local spins remain.

C. θ-(BEDT-TTF)$_2$CsZn(SCN)$_4$

The resistivity of the CsZn salt decreases with decreasing temperature and has a minimum at ≈ 100 K, below which the resistivity exhibits an upturn.[6,18] The resistivity depends slightly on the cooling rate at $T<100$ K.[30] The x-ray measurements[31,32] reveal that the diffuse rods at $q=(2/3,k,1/3)$ and $(0,k,1/2)$ grow at $T\leq 120$ K, although the structural correlation length of these modulations are short (5–7 nm). Below 50 K, the $(0,k,1/2)$ intensity increases but the structural correlation length at 20 K remains less than 20 nm along each axis, indicating short-range charge order. The optical conductivity and Raman spectra at 6–300 K measured by Suzuki *et al.*[28] also suggest a short-range charge order of small amplitude. In addition, the ^{13}C-NMR measurements carried out by Chiba *et al.*[33] indicate that static charge disproportionation develops as temperature decreases below ≈ 140 K but that the disproportionation ratio is reduced again below ≈ 20 K. ^{13}C-NMR measurements of the CsZn salt were also done by Kodama *et al.*[30]

As the temperature is decreased, the spin susceptibility slowly decreases at $20\leq T\leq 300$ K but rapidly increases at $T\leq 20$ K.[34] The Curie-Weiss behavior in the low temperature regime is considered to be intrinsic. The spin concentration is 1% if we assume $S=1/2$ localized spins with $1\mu_B$. Nakamura *et al.*[34] proposed that spin singlets are formed in most sites but some sites remain that have a local paramagnetic spin, similar to the case of the rapidly cooled RbZn salt.

D. Theory

The insulating behavior observed in the BEDT-TTF crystals with 3/4-filled bands has been understood basically as charge ordering predicted in the extended Hubbard model with on-site and nearest-neighbor Coulomb repulsions. Quantum chemistry calculations indicate on-site Coulomb energy $U=4-6$ eV and nearest-neighbor Coulomb energy $V=2-3$ eV.[35–38] The BEDT-TTF layer of θ-(BEDT-TTF)$_2X$ is usually modeled as an anisotropic triangular lattice or equivalently as a square lattice with not only nearest-neighbor transfer integral t_p and Coulomb repulsion V_p but also with transfer integral t_c and Coulomb repulsion V_c along one of the diagonals [Fig. 1(b)]. The diagonal corresponds to the c axis in the actual crystal. It is considered that $|t_p|>|t_c|$ and $V_p\approx V_c$.

Seo examined the stability of possible charge-order patterns called vertical, diagonal, and horizontal stripes for various values of the parameters within mean-field approximation.[39] A slave-boson study[40] on the model that does not include V_c and exact diagonalization studies[41,42] were also undertaken. Mori first pointed out the possibility of nonstripe charge ordering called "threefold charge ordering" in the limit of zero transfer integrals $(t_p=t_c=0)$.[43] The stability of the threefold charge ordering in the extended Hubbard model was investigated within mean-field approximation.[44] Watanabe and Ogata found that stripe and threefold charge orders compete for $t_c/t_p=0$ and $V_p/t_p\approx V_c/t_p\approx 1-3$ using a variational Monte Carlo method, and suggested that the two diffuse rods observed in the CsZn salt correspond to the coexistence of the different charge orders.[45] Phase diagrams have been obtained using different approximations.[46,47] In addition, the stability of different charge orders under an electric field has been investigated.[48] Incidentally, Udagawa and Motome proposed that the two diffuse rods emerge from two different instabilities, Wigner crystallization due to off-site Coulomb repulsions and charge-density-wave instability due to Fermi-surface nesting.[49] Tanaka and Yonemitsu[50] and Miyashita and Yonemitsu[51] investigated the effect of electron-lattice couplings, which was found to be crucial to stabilize the horizontal stripe observed in the RbZn salt.

Note that these theories include nearest-neighbor Coulomb interactions but do not include more distant Coulomb interactions. However, calculations done by Mori[38,43] indicate that the next-nearest-neighbor Coulomb energies are as large as 1–2 eV, which are on the same order as those of the nearest-neighbor. Kuroki pointed out the importance of such long-range Coulomb interactions: he proposed that the cooperation between long-range Coulomb interactions including those of next-nearest-neighbor and Fermi-surface nesting can explain the diffuse rods $(2/3,k,1/3)$ observed in the CsZn salt and $(1/3,k,1/4)$ observed in the RbZn salt.[52]

III. EXPERIMENTAL METHOD

Single crystals of the CsZn and RbZn salts were synthesized using a standard electrochemical method.[18] We used an 8:2 mixture of 1,1,2-Trichloroethane and methanol as a solvent to dissolve M(SCN) and Zn(SCN)$_2$, instead of using 18-crown-6 ether.[18] The typical dimensions of the CsZn crystals were 100 μm$\times$20 μm$\times$1 mm, and those of the RbZn crystals were 500 μm$\times$300 μm$\times$1 mm along the a, b, and c axes. We cut some of the CsZn crystals along the a-b plane into small pieces.

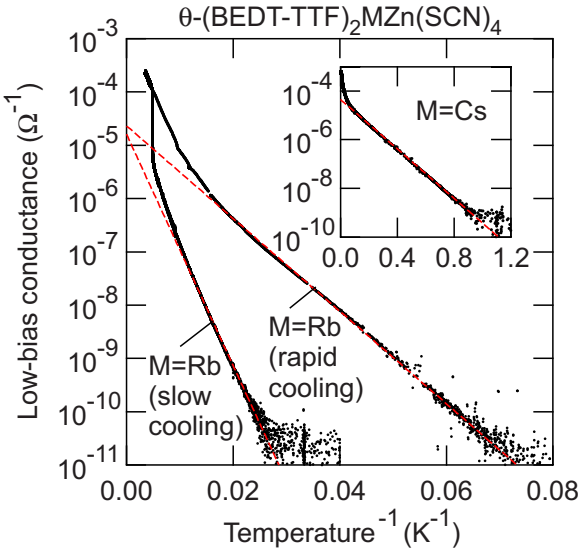

FIG. 2. (Color online) In-plane low-bias conductance of a CsZn crystal (electrode spacing $L=20$ μm; $V\|c$; $V=\pm 1$ mV for $T^{-1} \leq 0.8$ K^{-1} and ± 0.2 mV for $T^{-1} \geq 0.8$ K^{-1}) and a RbZn crystal ($L=10$ μm; $V\|a$; $V=\pm 1$ mV) as a function of inverse temperature. The dashed (red) lines are fits to the Arrhenius law.

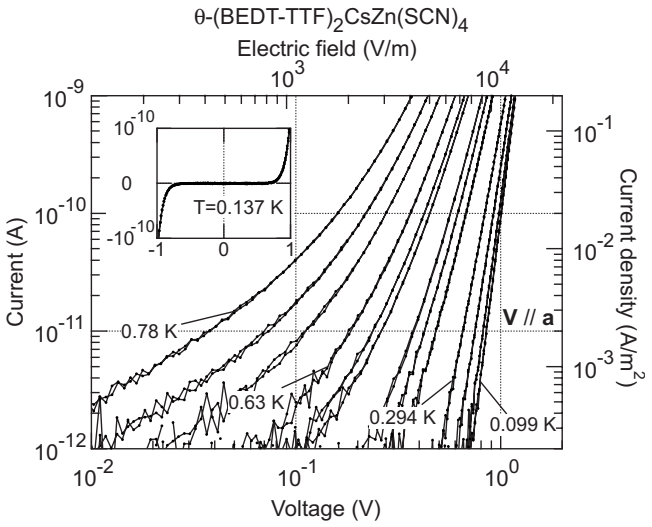

FIG. 3. In-plane (a-axis) I-V curves of a CsZn crystal. $T=0.78$, 0.73, 0.69, 0.63, 0.59, 0.57, 0.49, 0.456, 0.418, 0.294, 0.213, 0.138, and 0.099 K from top left to bottom right. The electrodes are attached to both sides of the crystal and the electrode spacing $L=90$ μm. Inset: I-V curve at 0.137 K on linear scale.

Annealed gold wires of 10 μm ϕ were attached with silver or carbon paste to a crystal surface parallel to the a-c plane (top electrodes; in-plane), or to both sides of a crystal (side electrodes; in-plane and out-of-plane). The typical spacing between the electrodes was 10–100 μm. We used silver paste in the initial stage of the study but it caused contact resistance that was larger than that for carbon paste and gradually increased when the sample was stored at room temperature. The crystals were cooled in a ^{3}He cryostat (Oxford Instruments or Cryogenic) or a dilution refrigerator (Oxford Instruments), equipped with a superconducting magnet. When measured in the ^{3}He cryostats (Figs. 2, 4, 8, 9, and 14), the crystals were surrounded by liquid ^{3}He at $T \leq 1.6$ K, and by ^{3}He gas at $T \geq 3$ K. The crystals were surrounded by a ^{3}He-^{4}He liquid mixture in all measurements we made in the dilution refrigerator (Figs. 3, 11–13, and 15).

The current-voltage characteristics were measured mostly with a two-point configuration. The voltage was applied using a function generator (Agilent Technologies, 33220A) or a source-measure unit (Keithley Instruments, 2400). The current was measured using a current preamplifier (Stanford Research Systems, SR570). In the high-bias region of some samples, we used a pulsed voltage technique to check how large power (=voltage × current) led to an obvious signature of self-heating, i.e., an increase in current during the voltage pulse. The data presented in this paper were obtained with a power that was less than such a critical value. A voltage pulse with a width of 50–250 μs was generated using the function generator. The output voltage of the current preamplifier was monitored using an oscilloscope (LeCroy, LT264). The time interval between successive pulses was 500 ms. We also did four-point measurements: We applied a voltage across the outer two electrodes and measured the current in the same way as the two-point method while we simultaneously measured the voltage across the inner two electrodes with an electrometer (Keithley Instruments, 6514). The input impedance of the electrometer is nominally $>10^{14}$ Ω. Such high-input impedance was required because the resistance of the crystal was high ($>10^{10}$ Ω) at low temperatures.

The magnetoconductance was measured in magnetic fields up to 17.5 T applied with a superconducting magnet. The temperature was kept constant during the magnetic field sweep with the following procedures: The temperature in the dilution refrigerator was controlled using a ruthenium oxide thermometer placed at the top part, which was inside a field-cancellation coil, of the mixing chamber. We used a resistance thermometer (Lake Shore Cryotronics, Cernox 1030) placed near the sample to control the temperature in the ^{3}He cryostats, at $T \geq 3$ K, at which the sample was surrounded by ^{3}He gas. Because of the magnetoresistance of the thermometer, the temperature shifts slightly at high magnetic fields. Calculations using the magnetoresistance data reported in Ref. 53 and the sensitivity $d \log R / d \log T$ of the thermometer we used indicate that the maximum shift of temperature is 3% at $B=17.5$ T at $3 \leq T \leq 15$ K. At $T \leq 1.6$ K, the sample was immersed in liquid ^{3}He. The temperature was held constant by keeping the vapor pressure constant in this temperature region. (The vapor pressure in the Oxford ^{3}He cryostat was kept constant by keeping the temperature of the sorption pump 0.5 m off the center of the magnet.)

The dielectric properties were measured using an *LCR* meter (Agilent Technologies, 4284A) at 1–100 kHz or a capacitance bridge (Andeen-Hagerling, 2500A) at 1 kHz with a two-point configuration. They were measured at temperatures down to 0.6 K using a ^{3}He jacket inserted into the Cryogenic variable temperature insert. To reduce parasitic capacitance between the measurement leads, we introduced stainless-steel coaxial cables (Lake Shore Cryotronics, type SS) to a measurement probe of the ^{3}He cryostat. The capacitance between the two leads measured without samples was

TABLE I. Parameters of ten CsZn crystals used for in-plane (*a*-axis) and out-of-plane (*b*-axis) dielectric measurements. *L* and *S* are the spacing and area of electrodes. The table lists values of capacitance *C* (and ϵ/ϵ_0) measured at 0.6 K (*0.7 K for samples Da2 and Db2) at 1 kHz. The capacitances for Da1–Da3 and Db1–Db3 were measured using the capacitance bridge. We note that the capacitances for Da4–Da6 and Db4 were measured with a different method from those described in Sec. III. They were measured using a combination of a current amplifier (FEMTO, DHPCA-100), a lock-in amplifier (NF, 5610B), and a function generator (Agilent Technologies, 33220A). Gold electrodes were evaporated onto both sides of the crystals for Da4 and Db4. (Carbon paste electrodes were used for Da1–Da3, Da5, Da6, and Db1–Db3.)

Sample name	Axis	L (μm)	S (μm^2)	C (0.6 K*)	ϵ/ϵ_0 (0.6 K*)
Da1	*a*	100	4.4×10^5	4.9×10^{-11}	1300
Da2	*a*	120	1.0×10^5	1.3×10^{-11}	1800
Da3	*a*	120	9.3×10^4	7.2×10^{-12}	1100
Da4	*a*	120	4.2×10^5	3.2×10^{-11}	1000
Da5	*a*	560	1.6×10^5	4.6×10^{-12}	1800
Da6	*a*	270	8.9×10^4	3.7×10^{-12}	1300
Db1	*b*	40	4.8×10^4	1.4×10^{-13}	13
Db2	*b*	60	7.6×10^4	1.5×10^{-13}	13
Db3	*b*	30	7.0×10^4	1.9×10^{-13}	9
Db4	*b*	150	2.8×10^5	2.2×10^{-13}	13

1×10^{-14} F, which showed negligible dependences on temperature (0.6–300 K), magnetic field (0–7.5 T), and frequency (1 kHz and 10–100 kHz). The raw values of the in-plane and out-of-plane capacitance were $\geq3.7\times10^{-12}$ F and $\geq1.4\times10^{-13}$ F (Table I), which were more than one order of magnitude larger than the value of the blank measurement.

IV. TEMPERATURE DEPENDENCE OF LOW-BIAS CONDUCTANCE

The in-plane conductance of the CsZn salt follows the Arrhenius law, $I/V=\exp(-\Delta_0/2k_BT)/R_0$, at $T<10$ K when the conductance is measured with a small bias voltage in a regime where the *I-V* curves are approximately linear (inset of Fig. 2). The activation energy Δ_0 is 23.5 ± 0.8 K for $V\|c$ (eight samples) and 24.2 ± 0.6 K for $V\|a$ (six samples); anisotropy in the *a-c* plane is negligible. The low-bias conductance along the *b* axis (out-of-plane direction) decreases slower than the Arrhenius law at temperatures down to ≈2 K. At $T=2.5$ K, the low-bias conductivity along the *b* axis is $10^{-5}-10^{-6}$ times that along the *c* axis, which indicates the highly 2D nature of the electrical transport.

The low-bias conductance of the RbZn salt depends on the cooling rate (Fig. 2): the conductance rapidly decreases at $T\approx190$ K when crystals are slowly cooled (0.06 K/min) but the rapid decrease in conductance disappears when they are rapidly cooled (>10 K/min). At sufficiently low temperatures, the conductances under both cooling conditions exhibit thermal activation behavior. The activation energy for slow cooling is 1010 ± 30 K for $V\|c$ (four samples) and 1020 ± 10 K for $V\|a$ (three samples), and that for rapid cooling is 410 ± 60 K for $V\|c$ (three samples) and 415 ± 5 K for $V\|a$ (two samples); again, no anisotropy can be seen in the *a-c* plane. The anisotropic charge modulation along the *c* axis indicated by x-ray and other measurements for the slowly cooled RbZn salt appears to have no influence on anisotropy in the low-bias conductance. We note that the saturation of the conductance in the low-temperature limit in Fig. 2 is due to the noise floor ($\approx10^{-13}$ A) in the current measurements.

V. HIGHLY NONLINEAR CURRENT-VOLTAGE CHARACTERISTICS

Figure 3 shows the current-voltage characteristics along the *a* (in-plane) axis of the CsZn salt measured at temperatures below 1 K. The *I-V* curves show high nonlinearity especially at lower temperatures. However, there is no clear threshold voltage for the higher conductivity as seen for the case of sliding conduction of the charge-density wave. In addition, there is neither significant hysteresis for increasing and decreasing voltage nor asymmetry between the bias polarities. At low temperatures, the *I-V* curve approximately follows the power law, $I\propto V^\alpha$, and the power exponent α is considerably large: $\alpha=8.2\pm0.3$ (two samples) at 0.3 K and 13.5 ± 0.4 (three samples) at 0.1 K for $V\|a$. The *c*-axis *I-V* characteristics are nearly the same as those along the *a* axis; $\alpha=8.5\pm0.2$ (nine samples) at 0.3 K and 15 (1 sample) at 0.1 K for $V\|c$. Measurements using different electrodes on a thin crystal showed that the voltage needed for a value of current was proportional to the spacing between the electrodes. In addition, using the four-point configuration, we obtained power-law *I-V* curves with the same exponents as those for the two-point configuration. These facts indicate that the power law is derived from from the nature of the crystal, not that of the interface between the crystal and the electrodes. The *b*-axis (out-of-plane) *I-V* characteristics show nonlinearity at electric fields 1–2 orders of magnitude higher than those for the in-plane *I-V* characteristics.

Both slowly and rapidly cooled RbZn salts exhibit similar nonlinear *I-V* curves as shown in Fig. 4. The *I-V* curves in

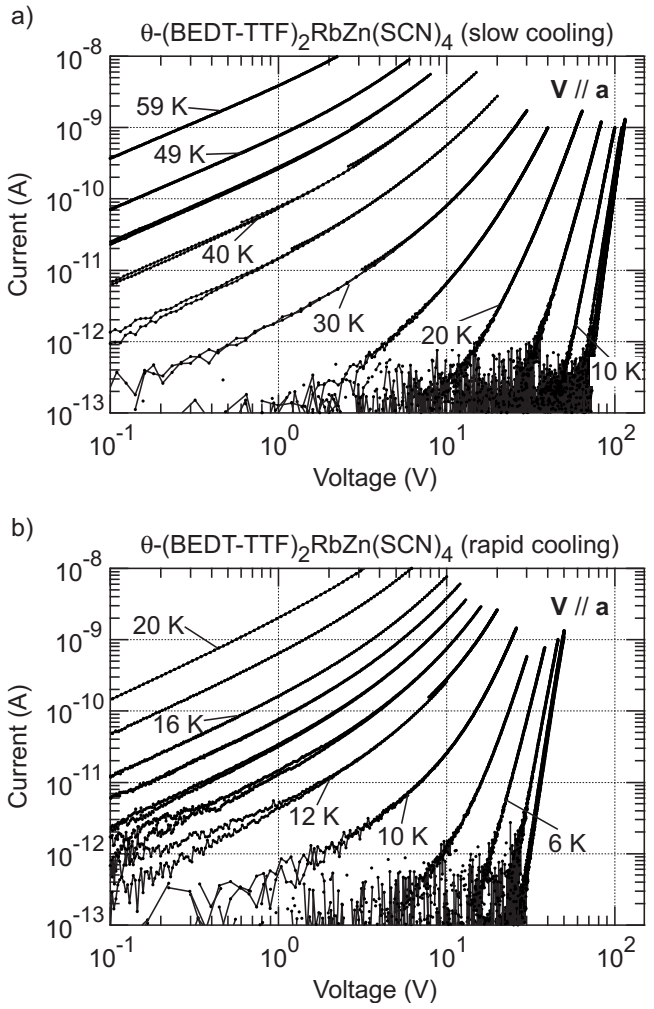

FIG. 4. In-plane (*a*-axis) *I-V* curves of a RbZn crystal under (a) slow-cooling and (b) rapid-cooling conditions. (a) $T=59.1$, 49.2, 44.3, 39.5, 34.6, 29.8, 24.9, 19.9, 14.9, 10.0, 6.01, 4.22, 3.51, 1.22, and 0.31 K from top left to bottom right. (b) $T=19.9$, 17.9, 15.9, 14.9, 13.9, 12.9, 11.9, 10.0, 7.99, 6.01, 3.51, 1.27, 0.55, and 0.33 K from top left to bottom right. The *I-V* curves in (a) and (b) were measured using the same pair of electrodes (with separation L of 10 μm) on the same crystal under different cooling conditions.

Figs. 4(a) and 4(b) were measured for the same electrode pair on the same crystal under different cooling conditions: first, the sample was cooled slowly at a rate of $\approx$0.06 K/min at 210–175 K and of $\approx$0.5 K/min at the other temperatures. Then, the *I-V* curves were measured at each temperature from the lowest to the highest [Fig. 4(a)]. After being warmed to 285 K, the sample was cooled rapidly at a rate of $\approx$18 K/min at 220–130 K and of $\leq$2 K/min at the other temperatures. The *I-V* curves were measured again from lower to higher temperatures [Fig. 4(b)]. For the sample in Figs. 2(b) and 2(c) of Ref. 54, we measured the *I-V* curves after slow cooling, after rapid cooling, and again after slow cooling. The dependence of the low-bias conductance on temperature and the *I-V* curves in the second slow cooling are nearly the same as those in the first slow cooling, which indicates that the differences in the *I-V* curves are not due to any degradation of the sample during the thermal cycle.

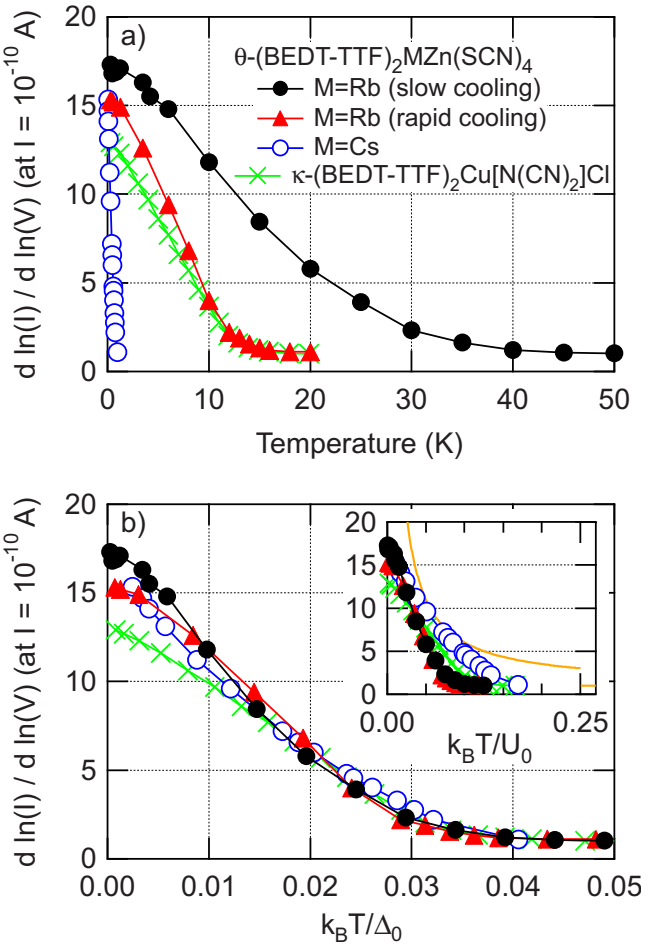

FIG. 5. (Color online) $d\ln(I)/d\ln(V)$ of the CsZn, and RbZn salts, and κ-(BEDT-TTF)$_2$Cu[N(CN)$_2$]Cl at $I=10^{-10}$ A plotted as a function of (a) temperature, (b) k_BT/Δ_0, and (inset of b) k_BT/U_0. $d\ln(I)/d\ln(V)$ of the CsZn and RbZn salts are obtained from the *I-V* curves in Figs. 3 and 4. Δ_0 is the activation energy obtained from the temperature dependence of low-bias conductance. U_0 is the coefficient of the logarithmic potential (see text). The solid (orange) line in the inset of (b) shows $U_0/2k_BT+1$ [the power-law exponent of Eq. (3)] for $k_BT/U_0<1/4$ and 1 for $k_BT/U_0>1/4$, where $T=U_0/4k_B\equiv T_{\mathrm{BKT}}$ is the Berezinskii-Kosterlitz-Thouless transition temperature.

The nonlinearity for slow cooling sets in at higher temperatures and at higher electric fields than that for rapid cooling. This appears to be related to the larger zero-bias activation energy Δ_0 for slow cooling. To quantitatively compare the *I-V* characteristics, we plotted $d\ln(I)/d\ln(V)$, i.e., the slope of the *I-V* curves in the log-log plot, at $I=10^{-10}$ A as a function of temperature in Fig. 5(a). At high temperatures, $d\ln(I)/d\ln(V)\approx 1$, which means that the *I-V* curve is Ohmic. With decreasing temperature, nonlinearity in the *I-V* curve develops, and $d\ln(I)/d\ln(V)$ therefore increases. The increase in $d\ln(I)/d\ln(V)$ occurs at higher temperatures in slow cooling than in rapid cooling. An important feature is that when the same data are plotted as a function of T/Δ_0, the data for both cooling conditions fall on nearly the same line as seen in Fig. 5(b). We have also plotted the $d\ln(I)/d\ln(V)$ of the CsZn salt at $I=10^{-10}$ A as

a function of T and T/Δ_0 in Fig. 5. Although the comparison is less direct than that between different cooling conditions for the single RbZn crystal, the $d\ln(I)/d\ln(V)$-T/Δ_0 curve of the CsZn salt is also close to those of the RbZn salt.

We also measured the I-V characteristics of κ-(BEDT-TTF)$_2$Cu[N(CN)$_2$]Cl, which is considered to be a Mott insulator. This salt also exhibits similar highly nonlinear I-V characteristics[17] and a similar $d\ln(I)/d\ln(V)$-T/Δ_0 curve [Fig. 5(b); $\Delta_0/k_B=380$ K]. These experimental results suggest that the nonlinear I-V curves of the CsZn salt and the RbZn salt under both cooling conditions, and κ-(BEDT-TTF)$_2$Cu[N(CN)$_2$]Cl have the same origin. Inagaki *et al.*[11] and Inada *et al.*[55] proposed that the nonlinear conduction in the CsZn and rapidly cooled RbZn salts is related to the coexistence of different charge-order patterns suggested for the CsZn and rapidly cooled RbZn salts. However, our experimental results described above are inconsistent with this proposal because there have been no experiments that have indicated the coexistence of different charge-order patterns in the slowly cooled RbZn salt and in κ-(BEDT-TTF)$_2$Cu[N(CN)$_2$]Cl. Another mechanism should be responsible for the nonlinear I-V curves at least in the low-bias region. We propose a simple model that explains the nonlinear I-V curves in the next section. Self-heating effects, which are another possible cause of the nonlinear I-V curves, will be examined in Sec. IX. We note that magnetoconductance data presented later provides evidence that self-heating effects are negligible.

VI. MODEL FOR NONLINEAR *I-V* CHARACTERISTICS

This section describes a simple model that explains the nonlinear I-V curves. The idea is very similar to the Poole-Frenkel effect in semiconductors and the mechanism for the nonlinear V-I curves in 2D vortex systems as will be explained later. For simplicity, let us consider an extended Hubbard model, $H=\Sigma_{\langle ij\rangle\sigma}t_{ij}c^{\dagger}_{i\sigma}c_{i\sigma}+U\Sigma_i n_{i\uparrow}n_{i\downarrow}+(1/2)\Sigma_{i\neq j,\sigma\sigma'}V_{ij}n_{i\sigma}n_{j\sigma'}$, in the limit of $t_{ij}\to 0$ and at half filling. Here, V_{ij} is a decreasing function of distance r_{ij} ($V_{ij}\to 0$ for $r_{ij}\to\infty$) and $U>V_{ij}$. In this case, the ground state is the Mott insulating state in which each site is occupied by an electron. An excitation can be created by removing an electron from one site and adding an electron to another site. If V_{ij} are zero, the excitation energy U_{ex} for the pair of doubly occupied and unoccupied sites (doublon and holon) is U irrespective of the distance r_{ij} between the doublon and the holon [Fig. 6(a)]. If V_{ij} are not zero, however, U_{ex} depends on the distance: $U_{ex}=U-V_{ij}$. The U_{ex} increases with increasing r_{ij}, which means a long-ranged attractive interaction between the doublon and the holon [Fig. 6(b)]. Because of this attractive interaction, doublons and holons excited at finite temperature form bound pairs. These pairs do not contribute to electrical conductivity; an activation energy $U_{ex}(r_{ij}\to\infty)(=U)$ is required to separate a pair into free carriers.

When an electric field E is applied, the activation energy decreases because the potential tilts, as shown in Fig. 6(d). The doublon and the holon are unbound due to thermal activation over the potential barrier $\Delta(E)$. $\Delta(E)$ is a decreasing function of the electric field, and therefore, more numbers of free carriers are created at higher electric fields. The dc conductivity is given by

$$J/E=\sigma_0\exp[-\Delta(E)/(2k_BT)], \tag{1}$$

where J is current density. The dependence of Δ on E and therefore the dependence of J on E are determined by the function $U_{ex}(r_{ij})$. It is worth noting that Δ for a longer-ranged interaction depends more strongly on E for the same value of U [Figs. 6(c) and 6(d)]. In other words, because the electric fields $-dU_{ex}/dr$ for longer-ranged potentials are smaller, they can be cancelled more easily by the applied electric field. We note that if the transfer integral is not zero, the effective Coulomb potential will become smaller than the bare potential in Fig. 6 as the system approaches the metallic phase. In addition, we considered the case of half filling but we think that a similar mechanism of nonlinear I-V curves can be applied to the charge-ordered state at 3/4 filling if the range of the Coulomb interaction is much longer than the distance between the neighboring BEDT-TTF molecules.

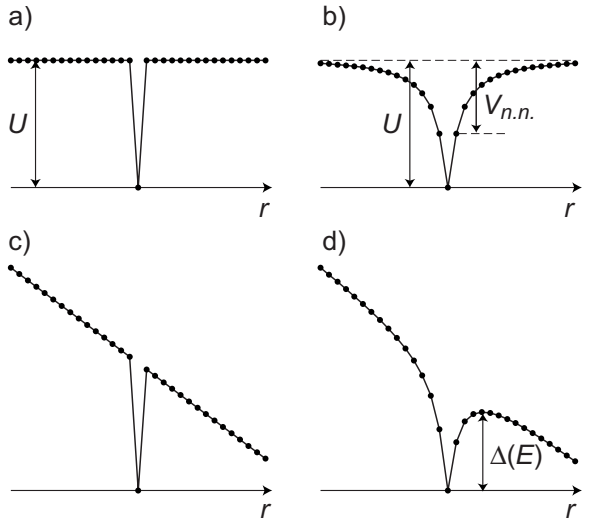

FIG. 6. (a) and (b) Excitation energy for a doublon-holon pair with a distance r for (a) $V_{ij}=0$ and (b) $V_{ij}\neq 0$. $V_{n.n.}$ denotes the nearest-neighbor V_{ij}. (c) and (d) Excitation energy under the applied electric field for (c) $V_{ij}=0$ and (d) $V_{ij}\neq 0$. $\Delta(E)$ is the activation energy to unbind a doublon-holon pair.

The experimentally obtained I-V curves follow a power law with an exponent that increases with decreasing temperature. Such power-law I-V curves can be explained by assuming that the Coulomb potential depends logarithmically on r: $U_{ex}=U_0\ln(r/a)$. For this potential,

$$\Delta(E)=\max[U_0\ln(r/a)-eEr]$$

$$\approx U_0\ln[U_0/(eEa)] \quad \text{for} \quad E\ll U_0/(ea). \tag{2}$$

This $\Delta(E)$ gives a power-law J-E curve,

$$J\approx\sigma_0(ea/U_0)^{U_0/(2k_BT)}E^{U_0/(2k_BT)+1}. \tag{3}$$

Figure 7 plots the I-V curves calculated from the above model to explain the I-V curves of the slowly cooled RbZn salt. The I-V curves of the CsZn salt and the rapidly cooled RbZn salt were also fitted to the model.[54] We assumed that

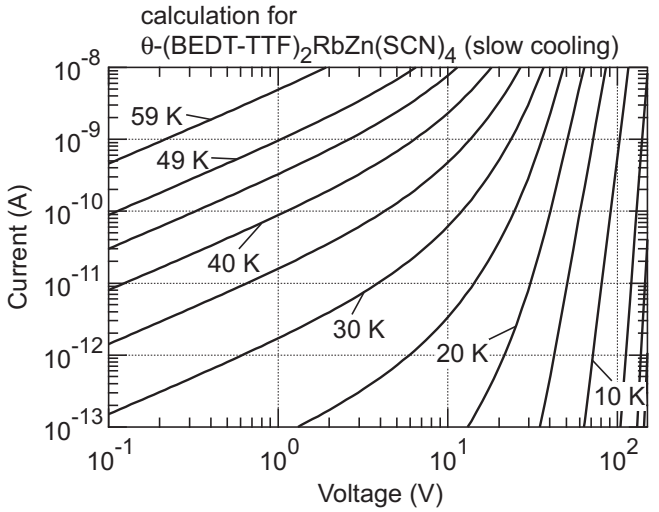

FIG. 7. Calculated *I-V* curves for the slowly cooled RbZn salt [Fig. 4(a)]. T=59.1, 49.2, 44.3, 39.5, 34.6, 29.8, 24.9, 19.9, 14.9, 10.0, 6.01, 4.22, and 3.51 K from top left to bottom right.

the potential was logarithmic in the distance at $r \leq \lambda$ and was constant at $r > \lambda$: $U_{ex} = U_0 \ln(r/a)$ at $a \leq r \leq \lambda$ and $U_{ex} = U_0 \ln(\lambda/a)$ at $r > \lambda$. We set the minimum length scale a as the distance (=0.5 nm) between the neighboring BEDT-TTF molecules and U_0 and λ as fitting parameters. The cutoff at λ makes the activation energy $\Delta(E)$ less sensitive to a small electric field and leads to the Ohmic part of the *I-V* curve at low biases. The crossover electric field from Ohmic to power-law characteristics is given by $U_0/(e\lambda)$. In addition, the activation energy Δ_0 obtained from the dependence of the low-bias conductance on temperature should correspond to $\Delta(E=0) = U_0 \ln(\lambda/a)$. Thus, the cutoff length λ (and U_0) can be determined from the crossover electric field and Δ_0. The best fits of the calculated *I-V* curves to those observed give $\lambda = 47 \pm 10$ nm (CsZn; ten samples), 5 ± 1 nm (RbZn; rapid cooling; five samples), and 7 ± 1 nm (RbZn; slow cooling; five samples). Because the distance between the neighboring BEDT-TTF molecules in the CsZn and RbZn salts is $\approx$0.5 nm, the values of λ mean that the Coulomb interaction is significantly long ranged. The values of U_0/k_B obtained by the fitting are 5.8 ± 0.4 K (CsZn; ten samples), 170 ± 10 K (RbZn; rapid cooling; five samples), and 400 ± 40 K (RbZn; slow cooling; five samples). Note that U_0 is the coefficient of the logarithmic potential and is not the on-site Coulomb energy.

We note that the density of the free charges normalized by the density of BEDT-TTF molecules is estimated to be less than 10^{-6} at the lowest temperatures even in the highest-bias region in our experiments (Figs. 3, 4, and 11). That is, the charge ordering itself is not influenced significantly by the electric field even in the highly nonlinear region. Along the lines of our model, one would expect that if the electric field was increased further, the charge gap would go to zero and it may change the ordered state into a different nonequilibrium state. Experimentally, however, self-heating effects hinder the temperature of the sample from being maintained at higher electric fields (see Sec. IX).

The experimental results show that the *I-V* curve has little dependence on temperature at low temperatures, i.e., at $T \leq 0.1$ K for the CsZn salt, at $T \leq 1.3$ K for the rapidly cooled RbZn salt, and at $T \leq 4.2$ K for the slowly cooled RbZn salt. Because of this small dependence of the observed *I-V* curve on temperature, the theoretical *I-V* curves deviate from the observed ones at the lowest temperatures. This small dependence on temperature may be explained by quantum tunneling from the tilted logarithmic potential, which should be dominant over the thermal activation process at low temperatures.

The logarithmic potential can be understood by assuming a superlattice of two alternating layers with different dielectric constants, corresponding to the BEDT-TTF and anion layers. If the dielectric constant ϵ_1 of the BEDT-TTF layer with the thickness of d_1 is much larger than the dielectric constant ϵ_2 of the anion layer with the thickness of d_2 ($\epsilon_1/\epsilon_2 \gg d_2/d_1$), the potential created by a charge in the BEDT-TTF layer is given by

$$\phi(r) \approx -\frac{2e}{\epsilon_1 d_1}\left[\ln\left(\frac{r}{2}\sqrt{\frac{\epsilon_2}{\epsilon_1 d_1 d_2}}\right) + C\right] \tag{4}$$

for $d_1 \ll r \ll \sqrt{d_1 d_2 \epsilon_1/\epsilon_2}$, where r is the distance in the BEDT-TTF layer from the charge and C is the Euler constant.[56] For $r \gg \sqrt{d_1 d_2 \epsilon_1/\epsilon_2}$, the potential decreases as $1/r$: $\phi(r) \approx (e\sqrt{d_2/d_1})/(\sqrt{\epsilon_1 \epsilon_2} r)$. Thus, the potential is logarithmic in the distance if the distance is shorter than the cutoff length, $\sqrt{d_1 d_2 \epsilon_1/\epsilon_2}$. If $\epsilon_1 \gg \epsilon_2$ and $d_1 \approx d_1$, the dielectric constant of the superlattice along the in-plane direction is approximately $\epsilon_1/2$ and that along the out-of-plane direction is approximately $2\epsilon_2$. Therefore, large anisotropy should be observed. We actually measured the dielectric constant of the CsZn salt and observed large anisotropy, as will be described in Sec. VII.

The above derivation of the power-law *I-V* curves [Eqs. (1)–(3)] is identical to that of the power-law *V-I* curves in the 2D vortex system below the Berezinskii-Kosterlitz-Thouless (BKT) transition temperature T_{BKT}.[57,58] At $T < T_{BKT}$, bound pairs of a vortex and an antivortex that attract each other due to logarithmic interaction are thermally excited. The current fed through the system unbind the vortex-antivortex pairs, resulting in the power-law *V-I* curves. The BKT transition of "charges" interacting with each other due to the logarithmic potential has been predicted for 2D Josephson-junction arrays or 2D metal dot arrays.[59–62] Experiments have been carried out in Josephson-junction arrays fabricated by lithography[63–65] and granular metal films;[66] however, the BKT transition in these systems seems to be obscured by the short cutoff length, influence of quasiparticles (in Josephson-junction arrays), or random offset charges.[65,67,68] We expect that correlated-electron insulating organic salts having a highly 2D character may be a new candidate for the BKT transition of charges. In the CsZn and RbZn salts, and κ-(BEDT-TTF)$_2$Cu[N(CN)$_2$]Cl, however, we only observed thermal activation behavior of the low-bias conductance, instead of the $\sigma \propto \exp[-2b/\sqrt{T/T_{BKT}-1}]$ dependence expected for the BKT transition, where b is a constant of order one and T_{BKT} is the transition temperature. In addition, the exponent of the power-law *I-V* curve did not show a clear jump from 1 to 3, which is expected at the BKT transition [see

inset in Fig. 5(b)]. The absence of the BKT transition may be due to the still short cutoff length or interlayer effects. A longer cutoff length requires larger dielectric anisotropy, which may be accomplished if the system is made closer to the metallic ground state, e.g., by applying uniaxial (*a*-axial) pressure.[69] (See Sec. VII.)

The activation energy in insulators induced by electron-electron Coulomb interactions is equivalent to the electron-hole (doublon-holon) binding energy. Therefore, the decrease in the binding energy due to the applied electric field creates free carriers as explained above. In contrast, the activation energy (band gap) in band insulators arises from electron-lattice interaction and is usually much larger than the exciton binding energy. Because the bottleneck for creating free carriers is the band gap, the decrease in the binding energy due to the applied electric field does not help to create free carriers. If there are shallow donor levels in a band insulator, however, the applied electric field assists the thermal escape of electrons from the shallow donors, causing nonlinear *I-V* curves (Poole-Frenkel effect). In the Poole-Frenkel model,[70] the 3D $1/r$ potential is used to derive the nonlinear *I-V* curve: $U_{ex}=U_0'a/r$ and therefore, $\Delta(E)\approx U_0'-2\sqrt{U_0'aeE}$.

VII. DIELECTRIC PROPERTIES

In previous sections, we treated dc *I-V* characteristics, which can be explained by the conduction of free charges created by the electric field induced unbinding of thermally excited electron-hole pairs. In addition to the free charges, there should also be electron-hole pairs that remain to be bound. Although the bound pairs make no contribution to dc conductivity, they should contribute to the dielectric constant. In this section, we present experimental results on the dielectric properties of the CsZn salt.

Figure 8 shows the temperature dependences of the in-plane and out-of-plane relative dielectric constants of the CsZn salt measured at 1, 10, and 100 kHz. The data at 1 kHz measured with the *LCR* meter and capacitance bridge have no significant difference. We note that the measured in-plane dielectric constant has little dependence on the ac excitation voltage and dc offset voltage in a voltage range in which the dc *I-V* curve is highly nonlinear. For the sample (Da3) whose in-plane dielectric constant is shown in Fig. 8, for example, the dc dynamic conductances dI/dV at $V=400$ and 700 mV are nearly one and two orders of magnitude larger than the value at $V=100$ mV at 0.6 K. However, the dielectric constants at 10 kHz at 0.6 K obtained for ac excitations of 10, 400, and 700 mV_{rms} are 98.3%, 114% and 139% of that obtained for the ac excitation of 100 mV_{rms}. In addition, the dc offset voltage of 700 mV leads to only a 10% increase in the dielectric constant for the ac excitation of 100 mV_{rms} at 10 kHz at 0.6 K.

There have been experiments on the dielectric properties of the CsZn salt at higher temperatures. The out-of-plane dielectric constant of the CsZn salt at 1 kHz$\leq f\leq$1 MHz at $4.3\leq T\leq 7.1$ K has been reported by Inagaki *et al.*[11] Although the reported dielectric constant is nearly twice that measured by us, its dependences on frequency and temperature are similar to ours. The in-plane dielectric constant of the CsZn salt at 10 kHz$\leq f\leq$10 MHz at $4.3\leq T\leq 300$ K has been reported by Nad *et al.*[71] We note that it is necessary to cool the sample below ≈1.6 K in our setup to accurately measure the in-plane dielectric constant because the dissipation factor $\tan(\delta)$ ($\equiv G/\omega C$; *C*: capacitance, *G*: parallel conductance) is significantly large above this temperature (Fig. 9). We measured six samples in the in-plane and four samples in the out-of-plane directions. They yielded results

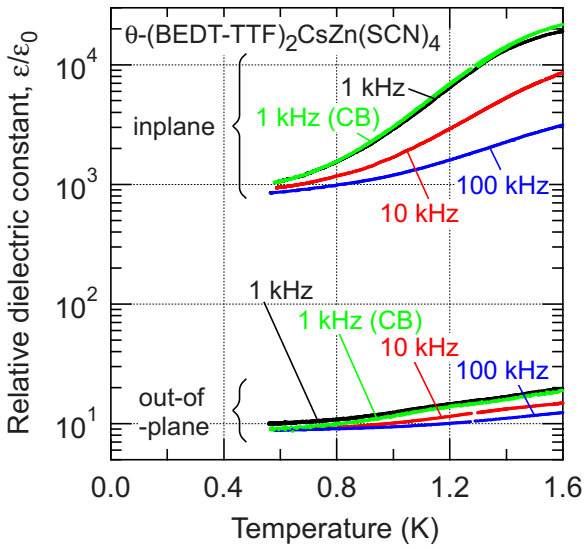

FIG. 8. (Color online) Temperature dependences of in-plane (*a*-axis) and out-of-plane (*b*-axis) relative dielectric constants of the CsZn salt (samples Da3 and Db3). The curves labeled CB were measured with the capacitance bridge while the others were measured with the *LCR* meter. The ac excitation voltages are 0.1 V_{rms} (*LCR* meter), 0.1 V_{rms} (CB, $T\leq 1.27$ K), and 0.03 V_{rms} (CB, $T\geq 1.29$ K) for the in-plane direction and 1 V_{rms} (*LCR* meter) and 0.75 V_{rms} (CB) for the out-of-plane direction.

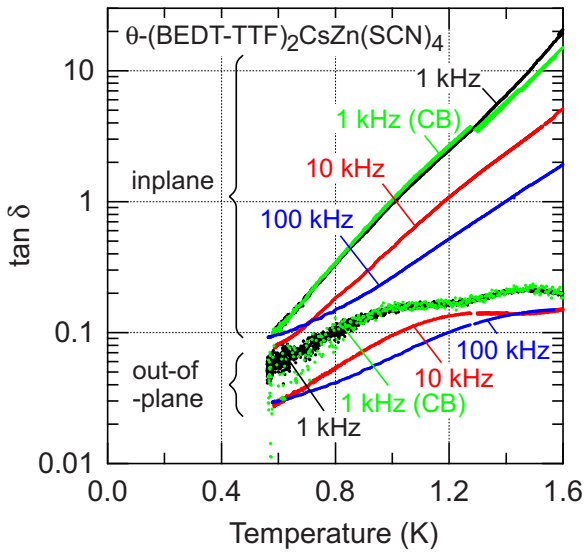

FIG. 9. (Color online) Temperature dependence of the dissipation factor, $\tan(\delta)$, of the CsZn salt (samples Da3 and Db3). The curves labeled CB were measured with the capacitance bridge while the others were measured with the *LCR* meter. The data were obtained at the same time as those in Fig. 8.

that are nearly the same as those in Figs. 8 and 9. Table I lists the sample dimensions and the dielectric constants at the lowest temperature. We found no significant differences between the carbon-paste and gold-film electrodes. In addition, the value of the dielectric constant along each crystal axis was nearly independent of the electrode spacing L, which varied by a factor of five. These facts indicate that the measured dielectric properties are intrinsic to the sample and not caused by the interface between the sample and the electrodes.

The in-plane dielectric constant is $\approx 1000\epsilon_0$-$20000\epsilon_0$ and the out-of-plane dielectric constant is $\approx 10\epsilon_0$-$20\epsilon_0$ in the temperature range of Fig. 8. These values correspond to an ϵ_1 of $2000\epsilon_0$-$40000\epsilon_0$ and an ϵ_2 of $5\epsilon_0$-$10\epsilon_0$ in the superlattice model described in Sec. VI. If we assume $d_1=d_2=1$ nm, the cutoff length $\sqrt{d_1 d_2 \epsilon_1/\epsilon_2}$ of the logarithmic potential is estimated to be $\approx$20-60 nm. This value is close to the value (=47 nm) estimated from the nonlinear I-V curves. Thus, the observed dielectric anisotropy suggests 2D long-range Coulomb interaction that is consistent with the nonlinear I-V curves. The coefficient of the logarithmic potential, $U_0 = 2e^2/(\epsilon_1 d_1)$, can also be calculated from the value of ϵ_1 to be $U_0/k_B \approx 10$-200 K. This value is larger than that (=5.8 K) estimated from the nonlinear I-V curves. This discrepancy may be due to the frequency range of the dielectric measurements; i.e., the in-plane dielectric constant in the low-frequency limit, relevant to explaining the dc nonlinear I-V curve, may be larger than those at 1–100 kHz and may give a smaller value of U_0.

The value $\approx 1000\epsilon_0$ of the in-plane dielectric constant in the low-temperature limit is notably large. This large dielectric constant is probably caused by the fact that the CsZn salt is close to the metallic phase. [Fig. 1(c)] An enhancement of the low-temperature dielectric constant has been reported when phosphorus-doped silicon approaches the metallic phase.[72] A more analogous case is La_2CuO_{4+y}, in which the in-plane dielectric constant increases and dielectric anisotropy is therefore enhanced as an insulator-to-metal transition is approached.[73] The scenario for an enhanced in-plane dielectric constant (enhanced dielectric anisotropy) as the system approaches the metallic phase is consistent with the fact that the cutoff length estimated from the nonlinear I-V curves of the CsZn salt is longer than that of the RbZn salt. In these respects, the assumption of two layers each with an isotropic dielectric constant in the superlattice model may be too simplistic. The dielectric constant of the BEDT-TTF layer itself is probably anisotropic, the magnitude of which is enhanced as the system approaches the metallic phase. Including the anisotropic dielectric constant in the BEDT-TTF layer to build a better model is a task for future research.

We next discuss how the temperature and frequency dependences of the in-plane dielectric constant can be understood using the model that explains the nonlinear I-V curves. The thermally excited bound pairs of an electron and a hole are polarized when a small electric field is applied, and they therefore contribute to the dielectric constant. Of the bound pairs, larger pairs make a larger contribution to the dielectric constant because they have larger dipole moments; the mean polarizability of a pair with a separation of r in two dimensions is given by $(er)^2/(2k_BT)$. However, large pairs are thermally excited only at high temperatures because of the large activation energy, $U_{ex}(r)=U_0 \ln(r/a)$. In addition, as explained in Appendix, the relaxation time τ of larger pairs should be longer; i.e., $\tau = r^2 k_B T/(2DU_0)$, where D is the diffusion constant. The dielectric constant is written as

$$\epsilon = \epsilon_0 + n_0 \int_0^\infty r dr \frac{(er)^2}{2k_BT} \frac{1}{1+i\omega\tau(r)} \times \exp\left[-\frac{U_{ex}(r)}{k_BT}\right] \Bigg/ \int_0^\infty r dr \exp\left[-\frac{U_{ex}(r)}{k_BT}\right], \quad (5)$$

where n_0 is the electron-hole density for $T \to \infty$. (See Appendix) Figure 10 shows the dependence of the dielectric constant on temperature calculated with this equation. Taking into consideration the contribution of the dielectric constant, which should be close to ϵ_0, of the anion layer with a thickness comparable to that of the BEDT-TTF layer, we showed half the calculated dielectric constant value in Fig. 10. The dielectric constant increases with increasing temperature because larger pairs are thermally excited but at high frequencies, the increase is gradual because only small pairs can respond to the electric field.

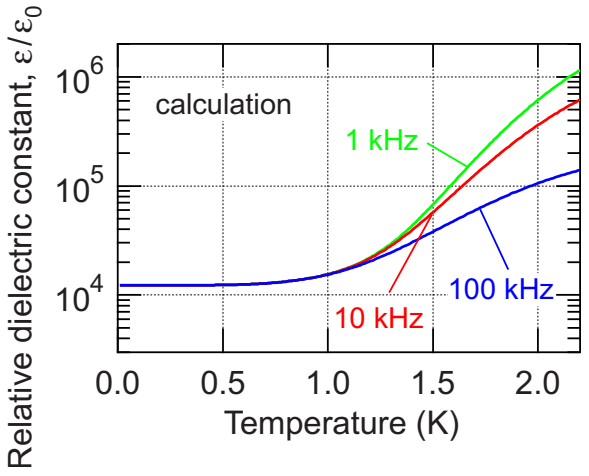

FIG. 10. (Color online) Temperature dependence of the in-plane relative dielectric constant calculated using Eq. (5).

Unlike the calculated I-V curve, the calculated dielectric constant especially at low temperatures (<1.5 K) is sensitive to the small-r part of the potential. We assumed in the calculation that the potential was proportional to r^2 near $r=0$ and was smoothly connected to $U_0 \ln(r/a)$ for large r; i.e., $U_{ex}(r)=U_0 r^2/(2r_C^2)$ for $0 \le r \le r_C$ and $U_{ex}(r) = U_0 \ln(r/a)$ for $r_C \le r \le \lambda$, where $r_C \equiv a\sqrt{\exp[1]}$. Such an r^2 potential at $0 \le r \le r_C$ would be created by a charge uniformly distributed within a sphere with a radius of r_C. We used the same values for the parameters of the logarithmic potential as those used to explain the nonlinear I-V curves; i.e., $U_0/k_B=5.8$ K, $\lambda=47$ nm, and $a=0.5$ nm. The upper limit of the integral in Eq. (5) was set to λ but even if we assume that the logarithmic potential is extended to $r \to \infty$ and set the upper limit to infinity, the results do not change much in the temperature range of Fig. 10. We took half the BEDT-TTF density as the electron-hole density for $T \to \infty$:

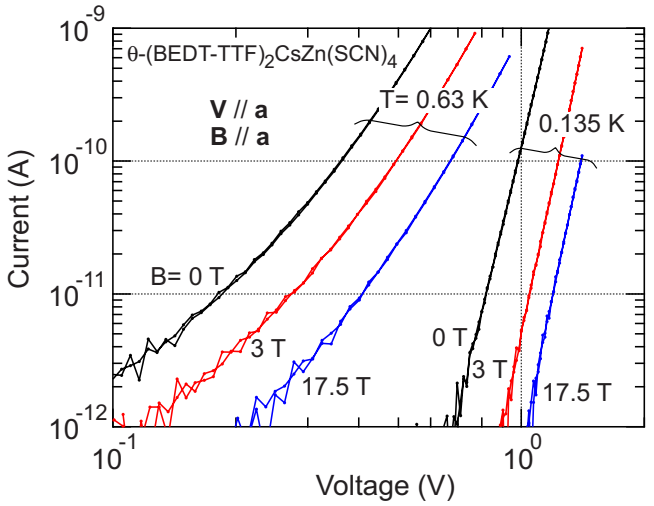

FIG. 11. (Color online) In-plane (*a*-axis) *I*-*V* curves of a CsZn crystal at $T=0.135$ and 0.63 K in magnetic fields of $B=0$, 3, and 17.5 T applied parallel to the *a* axis. The electrode spacing $L=90$ μm.

$n_0=1\times10^{27}$ (m^{-3}). The diffusion constant was obtained with the equation: $D=k_BT\sigma_0/(n_0e^2)=4\times10^{-12}\times T$ (m^2/s), where σ_0 was obtained from a fitting of the Arrhenius law, $\sigma=\sigma_0\exp(-\Delta_0/2k_BT)$, to the temperature dependence of the low-bias conductivity. Although the absolute value of the calculated dielectric constant is an order of magnitude larger than that of the measured value, which might be due to an overestimate of n_0, the calculation qualitatively explains the temperature and frequency dependences of the dielectric constant. Note again that the calculation was done using the same values for the parameters as those used to explain the nonlinear *I*-*V* curves. Thus, both the nonlinear *I*-*V* curve and dielectric properties can be understood within the context of the same model.

VIII. LARGE POSITIVE MAGNETORESISTANCE

This section describes the effect of the magnetic field on charge transport. Figure 11 shows the in-plane *I*-*V* curves of the CsZn salt measured in different magnetic fields. The *I*-*V* curves shift toward lower current in the log-log plot as the magnetic field is increased. The direction of the shift can be determined by examining the slope of the *I*-*V* curves in the log-log plot, i.e., $d\ln(I)/d\ln(V)$ (Fig. 12). The $d\ln(I)/d\ln(V)$ for the different magnetic fields fall on a single curve when plotted against voltage but not when plotted against current. This means that the application of the magnetic field shifts the *I*-*V* curve along the current axis in the log-log plot. That is, the magnetoconductance ratio, $I/I(B=0)$, for a fixed voltage does not depend on voltage; the magnetoconductance ratio in the high-voltage nonlinear region of the *I*-*V* curve is the same as that in the low-voltage Ohmic region (see also Fig. 1 of Ref. 74).

Let us consider the meaning of this voltage independence of the magnetoconductance effect within our model of the nonlinear *I*-*V* curve. The decrease in current means that the magnetic field decreases σ_0 or increases $\Delta(E)$ in Eq. (1). If Δ is a function of B, the magnetoconductance ratio $J(E,B)/J(E,B=0)$ generally depends on E unless $\Delta(E,B)$ is written as the sum of a term containing E and a term containing B. For example, if U_0 in Eq. (2) was a function of B, $J(E,B)/J(E,B=0)$ would depend on E. In contrast, $J(E,B)/J(E,B=0)$ is independent of E if only σ_0 depends on B. Thus, the voltage independence of the magnetoconductance effect suggests that the magnetic field decreases the mobility or the number of conduction paths, not the density (activation energy), of the free carriers.

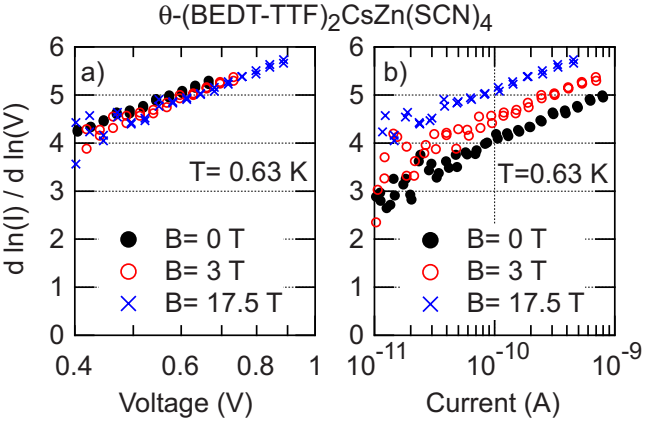

FIG. 12. (Color online) $d\ln(I)/d\ln(V)$ of the CsZn salt for $T=0.63$ K plotted as a function of (a) voltage and (b) current.

Figure 13(a) shows the dependence of current on magnetic field measured while the voltage was kept constant. Both the voltage and the magnetic field were applied along the *a* axis, which means longitudinal magnetoconductance. For $T=0.135$ K, data for $B\|c$ (transverse magnetoconductance) are also shown. The magnetoconductance curve depends little on the direction of the magnetic field. We note that the magnetoconductances for $B\|c$ and $B\|b$ are also close to each other.[74] The fact that the transverse and longitudinal magnetoconductances are nearly the same despite the highly 2D charge transport suggests that the magnetoconductance is not caused by orbital effects but is spin related. The four-probe measurement of magnetoconductance confirms that this is the magnetoconductance effect from the bulk of the sample, not that from the interface between the sample and electrodes. Another notable feature of the in-plane magnetoconductance is that it scales with μ_BB/k_BT as shown in Fig. 13(b). We found that the magnetoconductance is described by a simple empirical function,

$$I(T,B)/I(T,B=0)=[\cosh(\mu_BB/k_BT)]^{-1/2} \quad (6)$$

or

$$I(T,B)/I(T,B=0)=1/[1+(\mu_BB/2k_BT)^2]. \quad (7)$$

We also observed that there was some magnetoconductance effect for the out-of-plane current. However, the magnitude of the out-of-plane magnetoconductance (i.e., magnetoconductance measured with the voltage along the *b* axis) of the CsZn salt was smaller than that of the in-plane magnetoconductance, e.g., at 0.6 K, $I(B=6\ \text{T})/I(B=0)=0.12-0.16$ for $V\|a$ and $B\|a$ or $B\|b$ or $B\|c$, or for $V\|c$ and $B\|a$ or $B\|c$

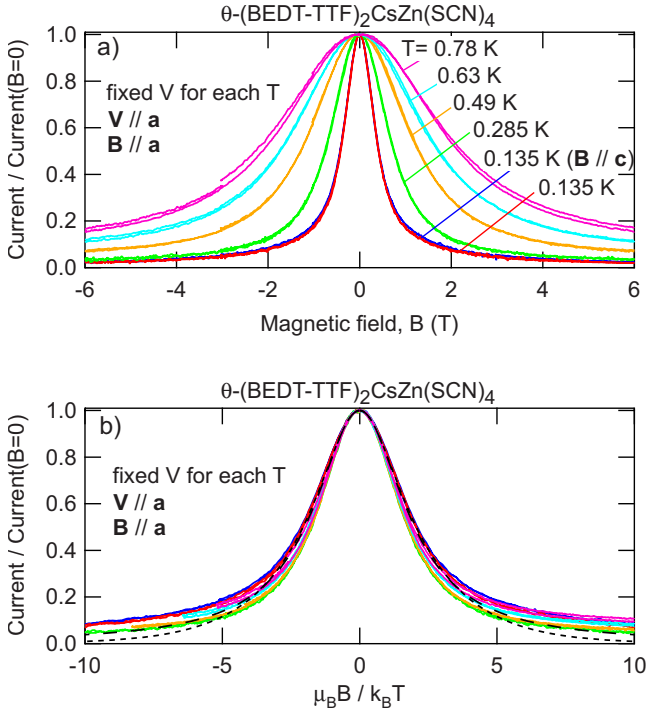

FIG. 13. (Color online) (a) Magnetic field dependence of current measured while voltage was kept constant in a CsZn crystal. The current is normalized to the value obtained in zero magnetic field at each temperature. Both the voltage and magnetic field were applied along the a (in-plane) axis so that orbital effects would be minimized. For $T=0.135$ K, data measured with $B\|c$ (the other in-plane axis) are also shown. Two curves for each temperature correspond to increasing and decreasing magnetic fields. (b) The same data are plotted as a function of $\mu_B B/k_B T$. The curves fall on a universal curve represented by $I/I(B=0)=[\cosh(\mu_B B/k_B T)]^{-1/2}$ (dotted line) or $I/I(B=0)=1/[1+(\mu_B B/2k_B T)^2]$ (dashed line).

[see Fig. 13(a)] but $I(B=6\ \mathrm{T})/I(B=0)=0.33-0.36$ for $V\|b$ and $B\|a$ or $B\|c$. In addition, there was a tendency for the in-plane magnetoconductance data measured with the side electrodes to remain to scale with $\mu_B B/k_B T$ down to lower temperatures than those measured with the top electrodes;[74] that is, the larger magnetoconductance effect was observed with the side contacts, for which the uniformity of current flow should be better than that for the top contacts. These results suggest that the in-plane current is more subject to the magnetic field effect than the out-of-plane current.

As described in Sec. II C, electron paramagnetic resonance and NMR measurements suggest that many of the electrons singly occupying the HOMOs of the BEDT-TTF molecules are paired into spin-singlet states at low temperatures but unpaired electrons remain that behave as localized paramagnetic spins. We expect that these paramagnetic spins will be located at the domain boundaries of charge order because the spin singlets will be disrupted at such boundaries. The free electrons created by electric field assisted thermal activation should encounter such localized spins when they flow through a sample with many domain boundaries. We note that the doublons and holons in Mott insulators are spinless, but the electrons and holes excited in the charge ordered state accompanied by spin singlets should have spin 1/2. The spin-carrying free charge can pass the localized spin site only when its spin and the localized spin are antiparalled; if they are parallel, the free charge cannot enter the localized spin site because of the Pauli exclusion principle. As the applied magnetic field is increased, the probability that two spins are parallel increases, and therefore, conductivity will be suppressed. The probability that two noninteracting spins are antiparallel is given by $p(T,B)=[\cosh(\mu_B B/k_B T)]^{-2}/2$. The observed universal function has a form similar to $p(T,B)$, implying a magnetoconductance effect induced by the Pauli exclusion principle.

The charge order in the slowly cooled RbZn salt is long ranged, and there will therefore be conduction paths that do not intersect domain boundaries accompanied by localized spins. The magnetoconductance effect of the RbZn salt is indeed smaller than that of the CsZn salt as shown in Fig. 14. Moreover, the magnetoconductance effect in slow cooling is smaller than that in rapid cooling. The magnetoconductance curves at $T\geq 3.5$ K become a function of $\mu_B B/k_B T$ close to Eq. (6) or (7) if an appropriate part of conductance is assumed to be independent of the magnetic field and is subtracted from the conductance (not shown). The magnetic field independent part of the conductance is attributed to the conduction paths that do not intersect the localized spin sites. The magnetoconductance effect of κ-(BEDT-TTF)$_2$Cu[N(CN)$_2$]Cl is even smaller than that of the slowly cooled RbZn salt.[17] This is consistent with the above scenario for the magnetoconductance effect because the magnetoconductane effect induced by the Pauli exclusion principle will not be applied to the spinless free charges in the Mott insulator.

The observed magnetoconductance effect is thus explained qualitatively but a full understanding requires further study. For example, although the magnetoconductance depends little on the direction of the magnetic field at low magnetic fields at which the data fall on the scaling function, some dependence is observed at high fields. Figures 15(a) and 15(b) show the dependences of $I/I(B=0)$ of the CsZn salt on the direction of the magnetic field. The angular dependences shown in Fig. 15(a) are similar to those measured while voltage was applied along the a axis and the magnetic field was tilted from b toward a [Fig. 6(a) of Ref. 74]. The figures indicate that the largest magnetoconductance effect is seen when the voltage and magnetic field are applied along the same in-plane direction. In addition, the smallest magnetoconductance effect is seen when the magnetic field is applied along the b axis. The origin of the dependence on the direction of the magnetic field needs to be clarified.

It has been reported that θ-(BEDT-TTF)$_2$CsCo(SCN)$_4$, which is analogous to the CsZn salt, also exhibits a positive magnetoresistance effect insensitive to the direction of the magnetic field, although no magnetoresistance curves have been published in the literature.[75] The insulating quasi-1D organic compound, $TTT_2I_{3-\delta}$, also exhibits a magnetoresistance ratio that follows $[R(B)-R(B=0)]/R(B=0)\propto(B/T)^2$ and that is independent of the direction of the magnetic field.[76] These may also be the magnetoconductance effects induced by the Pauli exclusion principle.

The positive magnetoresistance in the CsZn and RbZn salts is in marked contrast to the negative magnetoresistance

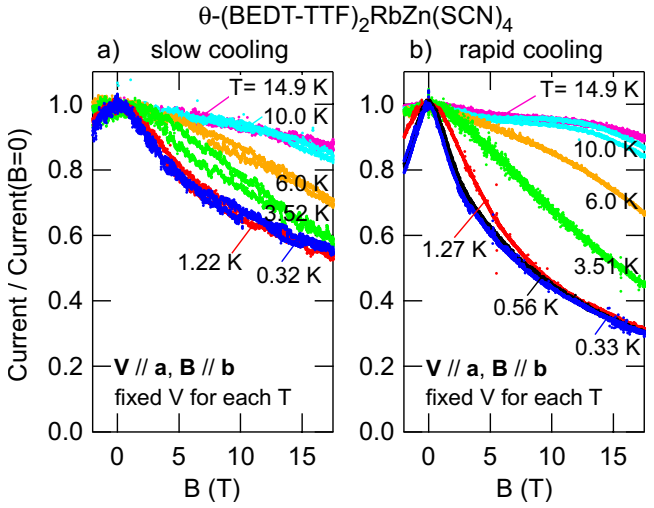

FIG. 14. .(Color online) Magnetic field dependence of current measured while voltage was kept constant for the same electrode pairs on a RbZn crystals under (a) slow- and (b) rapid-cooling conditions. The voltage was applied along the *a* axis and the magnetic field was applied along the *b* axis.

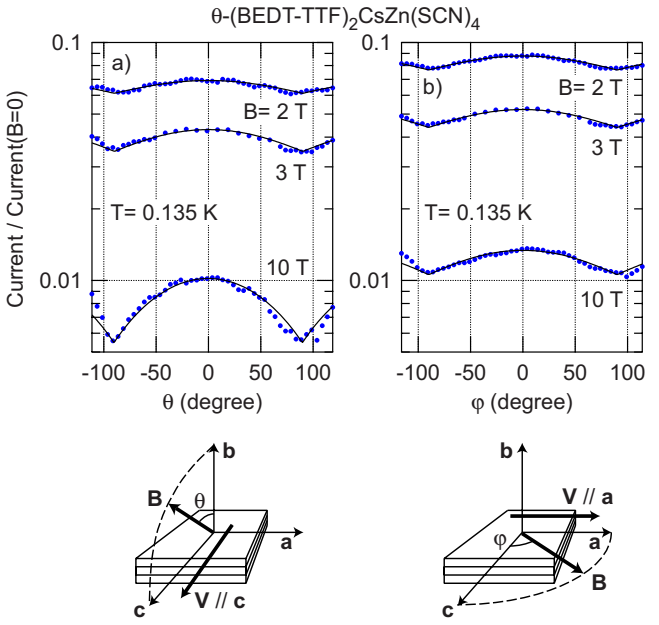

FIG. 15. (Color online) Dependence of $I/I(B=0)$ of the CsZn salt on the direction of the magnetic field at 0.135 K. (a) The voltage was applied along the *c* axis, and the magnetic field was tilted by θ from *b* toward *c*. The solid lines are fits to the formula, $I(B,\theta)/I(B,\theta=90°)=1+A(B)|\cos(\theta)|$. (b) The voltage was applied along the *a* axis, and the magnetic field was tilted by ϕ from *c* toward *a*. The solid lines are fits to the formula, $I(B,\phi)/I(B,\phi=90°)=1+A(B)|\cos(\phi)|$.

in manganite perovskites.[77] Conduction electrons and localized spins in manganite perovskites are on different *d* orbitals of Mn, and Hund's coupling is considered to be crucial for the magnetoresistance; namely, the magnetic field aligns the localized spins, which effectively enhances the transfer of the conduction electrons between neighboring sites. In contrast, in the CsZn and RbZn salts, both the conduction electrons and localized spins are on the HOMOs of the BEDT-TTF molecules; hence, the Pauli exclusion principle should be important. Positive magnetoresistance caused by the Pauli exclusion principle in a variable-range hopping regime has been investigated theoretically.[78,79] At zero magnetic field, a hopping process is allowed with a probability of 1/2 from an singly occupied site to another singly occupied site. In high magnetic fields, however, the spins are aligned and this process is prohibited due to the Pauli exclusion principle, thus leading to the positive magnetoresistance. Other hopping processes are allowed even in high magnetic fields, and the magnetoresistance therefore saturates to a certain value. The magnetoresistance ratio of the CsZn salt, e.g., obtained from the data in Fig. 13, does not saturate and becomes larger than that predicted in Ref. 78 at high magnetic fields. It appears that the theories cannot be applied directly to explain our experimental results but they may be helpful to construct a complete theory for the magnetoconductance phenomenon presented in this paper. Suppressed conductance due to the cooperation of the Pauli exclusion principle and the Coulomb-blockade effect has been observed in coupled quantum dots with an electron trapped in one dot.[80] Contrary to the case of the CsZn and RbZn salts, the application of high magnetic fields to this system increases the conductance because the conduction in high magnetic fields involves a higher-energy level that is different from the one that the trapped electron occupies.

IX. EVALUATION OF JOULE HEATING

Self-heating effects often lead to spurious nonlinear *I-V* curves. This section discusses estimates of the temperature increase in the organic crystals due to self heating, which we found to be negligible.

First, it is worth emphasizing that some features of the observed magnetoconductance indicate that the effect of self heating is small. The magnetoconductance, which was measured in the highly nonlinear region of the *I-V* curves at low temperatures, scales with $\mu_B B/k_B T$. Whatever the mechanism for this scaling is, it suggests that the temperature of the electronic system in the sample is identical to the bath temperature measured with a thermometer. This means that the nonlinearity of the *I-V* curve is not caused by the self-heating effect. The fact that the magnetoconductance is independent of voltage also suggests that the temperature increase due to the self-heating is negligible. If the temperature increased at high biases, the magnetoconductance would also decrease at the high biases.

The increase in the temperature of the sample due to self heating can be estimated using the thermal properties of the sample, liquid helium, and gold wires. Because the shapes of the samples, the ways electrodes (top or side electrodes) were attached, and coolants (^{3}He or ^{3}He—^{4}He mixture) differed in each measurement, we have to consider each case individually. We also have to consider self heating at each temperature because the path of thermal flow depends on temperature. Here we will consider two cases.

Let us first consider the CsZn salt immersed in ^{3}He—^{4}He mixture at 0.1 K (Figs. 3, 11–13, and 15). In these measurements, we attached electrodes on both sides of a small piece of a crystal with the electrode spacing ≈ 100 μm. The thermal conductivity of the dilute mixture of ^{3}He in ^{4}He at 0.1 K

is moderately large [≈ 0.05 W K^{-1} m^{-1} (Ref. 81)]. At 0.1 K, however, the thermal boundary resistance (Kapitza resistance $R_K \propto T^{-3}$) is so large that it prevents Joule heat from flowing directly from the sample to liquid helium. The temperature difference ΔT at the interface is given by

$$\frac{P_s}{A_s} = \int_{T_b}^{T_b+\Delta T} \frac{1}{R_K(T)} dT, \tag{8}$$

where $P_s = IV$ is the power dissipated in the sample, A_s is the surface area of the sample, and T_b is the temperature of the mixture close to the sample. We do not know the exact value of Kapitza resistance R_K between our samples and the ^{3}He—^{4}He mixture but it will be on the order of $(0.001-0.01) \times T^{-3}$ Km^2/W.[81] For $T_b = 0.1$ K, $P_s = 10^{-9}$ W, and $A_s = 10^{-7}$ m^2, ΔT is 0.01–0.05 K, which is not negligible compared to T_b. The heat should escape in the most part through the gold wires used for electrical measurements. Two gold wires 10 μm in diameter and 0.5–1.2 mm in length were attached to the sample with carbon paste. The other end of the wires was attached to an epoxy substrate with silver paste. (Gold wires 30 μm in diameter and 2–4 mm in length were extended between the epoxy substrate and electrodes on a sample holder.) Because the surface area of the silver paste on the epoxy substrate is large, we assume that the temperature of the gold wires ϕ 10 μm at the substrate is the same as the temperature T_0 of the mixing chamber. The temperature T_1 at the sample can be calculated from the power $P_s = IV$ dissipated in the sample and the thermal conductivity κ_{Au} of the gold wires,

$$\int_{T_0}^{T_1} \kappa_{\mathrm{Au}} dT = \frac{P_s}{2S_{\mathrm{Au}}} l_{\mathrm{Au}}. \tag{9}$$

(The 2 in the denominator on the right hand side corresponds to the two gold wires.) If we use $l_{\mathrm{Au}} = 1 \times 10^{-3}$ m, $S_{\mathrm{Au}} = 8 \times 10^{-11}$ m^2, $T_0 = 0.1$ K, and $\kappa_{\mathrm{Au}}/T = 60$ (W/K^2 m),[82,83] then $T_1 = 0.101$ K for $P_s = 10^{-9}$ W and $T_1 = 0.11$ K for $P_s = 10^{-8}$ W. Thus, the temperature increase is negligible if the power is less than 10^{-9} W.

We note that we should also consider the possibility of a temperature gradient inside the sample. The temperature gradient has been reported to cause nonlinear I-V characteristics in manganite perovskites.[84] The equations to determine the distribution of temperature, current density, and electric field inside the sample are

$$C_s \frac{\partial T}{\partial t} = \vec{\nabla} \cdot \kappa_s \vec{\nabla} T + \vec{j} \cdot \vec{E}, \tag{10}$$

$$\vec{j} = \sigma \vec{E}, \tag{11}$$

and Maxwell's equations.[85] Here, C_s and κ_s are the heat capacity and thermal conductivity of the sample. We assume that electrodes that act as a thermal bath at temperature T_1 are attached to a rectangular sample at both ends ($z = L/2$ and $-L/2$). In this case, the current density j should be uniform and along the z direction. The steady-state form of the above equations becomes

$$\frac{d}{dz}\left\{ \kappa_s[T(z)] \frac{dT(z)}{dz} \right\} + jE(z) = 0, \tag{12}$$

$$\sigma[T(z), E(z)] E(z) = j. \tag{13}$$

$T(z)$, $E(z)$, and $I = \int\int j dx dy$ are calculated by solving these equations under the boundary condition,

$$\int_{-L/2}^{L/2} E(z) dz = V. \tag{14}$$

As the thermal conductivity of the present salts has not been reported, we use the phonon thermal conductivity $\kappa \approx T^3$ (W K^{-1} m^{-1}) of other BEDT-TTF salts.[86,87] If we assume that σ depends only on temperature $\{\sigma = \sigma_0 \exp[-\Delta_0/(2k_B T)]\}$, a numerical calculation of the above equations shows that T is approximately the same as T_1 for $-L/2 \le z \le L/2$ and I is proportional to V. Thus, the observed nonlinear I-V curves cannot be explained by local Joule heating far from the electrodes inside the sample. The I-V curves at 0.138–0.294 K in Fig. 3 are described approximately by the equation $J = 10^{-66.9+92.3T} E^{16.0-21.8T}$. That is, $\sigma(E,T) = 10^{-66.9+92.3T} E^{15.0-21.8T}$. The numerical calculation for $T_1 = 0.138$ K using this $\sigma(E,T)$ shows that the temperature increase at the center of the sample is 1 mK for $V = 1.17$ V($I = 10^{-9}$ A) and 10 mK for $V = 1.40$ V($I = 10^{-8}$ A). Thus, the local heating at the center of the sample is negligible for $P_s = IV = 10^{-9}$ W.

Next, we will consider self heating of a RbZn crystal immersed in liquid ^{3}He at 0.3 K (Figs. 4 and 14). The electrodes for this measurement were attached with a small separation (=10 μm) on a surface parallel to the a-c plane of a relatively large crystal. If we assume that the Joule heat escapes through the Au wires as was discussed above, temperature T_1 at the sample is 0.317 K for $P = 5 \times 10^{-8}$ W. Joule heat is also conducted through the sample and escapes directly to the liquid ^{3}He via the surface of the sample. Let us consider a simplified model of thermal flow: Joule heat P occurs at the center within radius of 10 μm of a spherical crystal of the RbZn salt with radius r_a of 300 μm, immersed in liquid ^{3}He that fills up to $r_b = 5$ mm, at which the temperature T_0 is fixed at 0.3 K. The temperature at the center is calculated to be 0.315–0.328 K for $P = 5 \times 10^{-8}$ W for the thermal conductivity of the RbZn salt, $\kappa_s = T^3$ W K^{-1} m^{-1}, the thermal conductivity of liquid ^{3}He, $\kappa_{^3\mathrm{He}} = 6 \times 10^{-3}$ W K^{-1} m^{-1},[81] and the Kapitza resistance between the RbZn salt and liquid ^{3}He, $R_K = (0.001-0.01) \times T^{-3}$ Km^2/W.[81] Thus, the temperature at the measured part of the sample is ≈ 0.32 K for $P = 1 \times 10^{-7}$ W if we take into consideration the thermal flow both through the Au wires and through liquid ^{3}He. The temperature is ≈ 0.304 K for $P = 2 \times 10^{-8}$ W and ≈ 0.38 K for $P = 5 \times 10^{-7}$ W. Thus, the temperature increase due to Joule heating is small when $P \le 10^{-7}$ W. Note that the nonlinearity in the I-V curves appears clearly even at $P \le 10^{-10}$ W (Fig. 4).

X. CONCLUSIONS

We have measured the *I-V* curves, dielectric constants, and magnetoconductances of the layered organic crystals θ-(BEDT-TTF)$_2M$Zn(SCN)$_4$ (M=Cs, Rb), in which charge order is considered to occur at low temperatures. The in-plane *I-V* curves follow the power law with large exponents, e.g., ≈8 at 0.3 K and 14–15 at 0.1 K for the CsZn salt (M=Cs). Comparisons of the same RbZn salt under rapid- and slow-cooling conditions show that the power-law exponent scales with temperature divided by the zero-bias activation energy Δ_0, which is ≈410 K for rapid cooling and ≈1010 K for slow cooling. A similar scaling is applied to the *I-V* curves of the CsZn salt ($\Delta_0/k_B \approx 24$ K) and those of the Mott insulator κ-(BEDT-TTF)$_2$Cu[N(CN)$_2$]Cl (Δ_0/k_B ≈380 K) as well. These results suggest that the nonlinear *I-V* curves of these organic crystals have the same origin. The nonlinear *I-V* curves are explained by a simple model considering the electric field induced unbinding of the electron-hole pairs excited in the charge order or in the Mott insulating state. The analysis of the nonlinear *I-V* curves indicates that the 2D Coulomb interaction between the electron and the hole, which should reflect the properties of the electron-electron interaction causing the charge order or the Mott insulating state, is considerably long ranged; the cutoff length is 5–47 nm, which is much longer than the size ≈0.5 nm of the BEDT-TTF molecules. This long-range 2D Coulomb interaction is consistent with the large dielectric anisotropy of ≈100 between the in-plane and out-of-plane directions observed at 0.6 K for the CsZn salt. Such a large anisotropy in the dielectric constant has not attracted much attention but it may be important for a full understanding of the charge ordering in the layered organic crystals. The temperature and frequency dependences of the in-plane dielectric constant of the CsZn salt are also explained by the polarization of the electron-hole bound pairs, consistently with the nonlinear *I-V* curves. We expect that correlated-electron insulators of organic salts will generally show nonlinear *I-V* curves due to the above mechanism.[88,89]

The CsZn and RbZn salts also show a large positive magnetoresistance, e.g., ≈10 000% for the CsZn salt in the magnetic field of 10 T at 0.1 K. Despite the highly nonlinear *I-V* characteristics, magnetoconductance is independent of applied voltage. This suggests that the magnetic field suppresses the mobility or the number of conduction paths, not the density (the activation energy), of unbound free charges. The magnetoconductance is also nearly independent of the direction of the magnetic field, indicating that it is not an orbital effect but is spin-related. Spin-related large magnetoresistance ratios have often been observed in systems containing magnetic elements such as Mn or Fe (Refs. 77, 90, and 91) but the CsZn and RbZn salts contain no magnetic elements. Moreover, the magnetoconductance scales with $\mu_B B/k_B T$. We suggest that the magnetoconductance is caused by magnetic field induced parallel alignment of spins of the unbound free charges and localized spins located at the domain boundary of the charge order, and by the resulting suppression of electrical conduction due to the Pauli exclusion principle. This magnetoconductance effect in the organic crystals may have implications for the study of spin-dependent charge transport. Apart from the physical significance, it provides a useful measure of self-heating effects. The fact that the magnetoconductance measured in the nonlinear region of the *I-V* curve scales with $\mu_B B/k_B T$ indicates that the temperature of the electronic system is close to that of the bath even in the nonlinear region and the nonlinearity is thus intrinsic.

ACKNOWLEDGMENTS

The authors acknowledge discussions with M. Nakamura, N. Yokoshi, H. Mori, M. Ogata, T. Mori, I. Terasaki, T. Nakamura, M. Watanabe, H. Fukuyama, P. Monceau, K. Kuroki, K. Yoshimi, T. Kato, M. Kodama, K. Kanoda, T. Kawamoto, Y. Takano, and K. Kodama, and technical support from K. Matsuzaki, M. Suzuki, K. Noda, Y. Ikemoto, K. Enomoto, M. Nishimura, and K. Tanaka. The authors also thank T. Arima and H. Kitano for useful comments on the dielectric measurements, and thank T. Kato, H. Kamimura, and A. Kurobe for helpful comments on the manuscript. This work was supported by Grants-in-Aid for Scientific Research, Grants No. 17740202 and No. 20740208, and Grant-in-Aid for Scientific Research on Innovative Areas, Grant No. 20110004, from MEXT, Japan.

APPENDIX

In this appendix, we derive the equation [Eq. (5)] for the dielectric constant due to the polarization of bound electron-hole pairs by following Ref. 92. The calculation described in Ref. 92 is based on the Berezinskii-Kosterlitz-Thouless picture; namely, it takes into account the screening effect on the Coulomb interaction caused by other bound pairs, which leads to a renormalized Coulomb interaction. Here, we consider a simple bare Coulomb interaction, assuming that the temperature is sufficiently low so that a very small number of pairs can be excited.

We write a Fokker-Planck equation for $\rho(r,\theta)$, the probability of finding an electron-hole pair with separation r and with angle θ to the applied small electric field $\delta\vec{E}\exp(i\omega t)$,

$$\frac{\partial \rho}{\partial t} = 2D\vec{\nabla}^2\rho - \frac{2D}{k_B T}\vec{\nabla}\cdot(\rho\vec{F}), \tag{A1}$$

$$\vec{F} = -\vec{\nabla}U_{ex}(r) + e\,\delta\vec{E}\exp(i\omega t). \tag{A2}$$

To calculate the linear response, we write

$$\rho(r,\theta) = \rho_0(r) + \delta\rho(r,\theta)\exp(i\omega t), \tag{A3}$$

$$\rho_0(r) = \rho_0^c \exp[-U_{ex}(r)/(k_B T)]. \tag{A4}$$

Substituting these expansions into Eq. (A1) and retaining linear terms, we obtain

$$\frac{i\omega}{2D}\delta\rho = \frac{\partial^2\delta\rho}{\partial r^2} + \frac{1}{r^2}\frac{\partial^2\delta\rho}{\partial\theta^2} + \left(\frac{1}{r} + \frac{1}{k_BT}\frac{\partial U_{ex}}{\partial r}\right)\frac{\partial\delta\rho}{\partial r} + \frac{1}{k_BT}\left(\frac{1}{r}\frac{\partial U_{ex}}{\partial r} + \frac{\partial^2 U_{ex}}{\partial r^2}\right)\delta\rho + \frac{e\,\delta E}{(k_BT)^2}\frac{\partial U_{ex}}{\partial r}\rho_0\cos\theta. \tag{A5}$$

As a first approximation, we assume $\delta\rho(r,\theta)$ to have a simple form

$$\delta\rho(r,\theta) = \rho_0(r)\frac{e\,\delta E r\cos\theta}{k_BT}g(\omega). \tag{A6}$$

Here, $g=1$ corresponds to the static response. By substituting Eq. (A6) into Eq. (A5), we obtain

$$\frac{i\omega r}{2D}g = -\frac{1}{k_BT}\frac{\partial U_{ex}}{\partial r}g + \frac{1}{k_BT}\frac{\partial U_{ex}}{\partial r}. \tag{A7}$$

Therefore,

$$g(\omega) = \frac{1}{1+i\omega\tau}, \tag{A8}$$

$$\tau \equiv \frac{r}{2D}k_BT\left(\frac{\partial U_{ex}}{\partial r}\right)^{-1}. \tag{A9}$$

For the logarithmic potential, $U_{ex}(r)=U_0\ln(r/a)$, we obtain

$$\tau = \frac{r^2}{2D}\frac{k_BT}{U_0}. \tag{A10}$$

We now calculate the mean polarization,

$$\langle P\rangle = \frac{n_0\int_0^{2\pi}d\theta\int_0^{\infty}rdr\rho(r,\theta)er\cos\theta}{\int_0^{2\pi}d\theta\int_0^{\infty}rdr\rho(r,\theta)} = \frac{n_0\int_0^{\infty}rdr\rho_0(r)\frac{(er)^2}{2k_BT}\frac{1}{1+i\omega\tau(r)}\delta E\exp(i\omega t)}{\int_0^{\infty}rdr\rho_0(r)}, \tag{A11}$$

where n_0 is the electron-hole density for $T\to\infty$. We therefore obtain the dielectric constant,

$$\epsilon = \epsilon_0 + \langle P\rangle/[\delta E\exp(i\omega t)] = \epsilon_0 + n_0\int_0^{\infty}rdr\frac{(er)^2}{2k_BT}\frac{1}{1+i\omega\tau(r)}\times\exp\left[-\frac{U_{ex}(r)}{k_BT}\right]\Bigg/\int_0^{\infty}rdr\exp\left[-\frac{U_{ex}(r)}{k_BT}\right]. \tag{A12}$$

[1] S. S. P. Parkin, E. M. Engler, R. R. Schumaker, R. Lagier, V. Y. Lee, J. C. Scott, and R. L. Greene, Phys. Rev. Lett. **50**, 270 (1983).
[2] H. Taniguchi, M. Miyashita, K. Uchiyama, K. Satoh, N. Mori, H. Okamoto, K. Miyagawa, K. Kanoda, M. Hedo, and Y. Uwatoko, J. Phys. Soc. Jpn. **72**, 468 (2003).
[3] Y. Shimizu, K. Miyagawa, K. Kanoda, M. Maesato, and G. Saito, Phys. Rev. Lett. **91**, 107001 (2003).
[4] N. Tajima, S. Sugawara, M. Tamura, R. Kato, Y. Nishio, and K. Kajita, EPL **80**, 47002 (2007).
[5] K. Miyagawa, A. Kawamoto, and K. Kanoda, Phys. Rev. B **62**, R7679 (2000).
[6] H. Mori, S. Tanaka, and T. Mori, Phys. Rev. B **57**, 12023 (1998).
[7] T. Komatsu, H. Sato, T. Nakamura, N. Matsukawa, H. Yamochi, G. Saito, M. Kusunoki, K.-i. Sakaguchi, and S. Kagoshima, Bull. Chem. Soc. Jpn. **68**, 2233 (1995).
[8] M. Tamura, H. Kuroda, S. Uji, H. Aoki, M. Tokumoto, A. G. Swanson, J. S. Brooks, C. C. Agosta, and S. T. Hannahs, J. Phys. Soc. Jpn. **63**, 615 (1994).
[9] K. Miyagawa, A. Kawamoto, Y. Nakazawa, and K. Kanoda, Phys. Rev. Lett. **75**, 1174 (1995).
[10] H. Kino and H. Fukuyama, J. Phys. Soc. Jpn. **64**, 2726 (1995).
[11] K. Inagaki, I. Terasaki, H. Mori, and T. Mori, J. Phys. Soc. Jpn. **73**, 3364 (2004).
[12] F. Sawano, I. Terasaki, H. Mori, T. Mori, M. Watanabe, N. Ikeda, Y. Nogami, and Y. Noda, Nature (London) **437**, 522 (2005).
[13] M. Watanabe, K. Yamamoto, T. Ito, Y. Nakashima, M. Tanabe, N. Hanasaki, N. Ikeda, Y. Nogami, H. Ohsumi, H. Toyokawa, Y. Noda, I. Terasaki, F. Sawano, T. Suko, H. Mori, and T. Mori, J. Phys. Soc. Jpn. **77**, 065004 (2008).
[14] T. Ito, M. Watanabe, K.-I. Yamamoto, N. Ikeda, Y. Nogami, Y. Noda, H. Mori, T. Mori, and I. Terasaki, EPL **84**, 26002 (2008).
[15] F. Sawano, T. Suko, T. S. Inada, S. Tasaki, I. Terasaki, H. Mori, T. Mori, Y. Nogami, N. Ikeda, M. Watanabe, and Y. Noda, J. Phys. Soc. Jpn. **78**, 024714 (2009).
[16] R. Kondo, M. Higa, and S. Kagoshima, J. Phys. Soc. Jpn. **76**, 033703 (2007).
[17] Y. Takahide, M. Kimata, K. Hazama, T. Terashima, S. Uji, T. Konoike, M. Kobayashi, and H. M. Yamamoto (unpublished).
[18] H. Mori, S. Tanaka, T. Mori, A. Kobayashi, and H. Kobayashi, Bull. Chem. Soc. Jpn. **71**, 797 (1998).
[19] M. Watanabe, Y. Noda, Y. Nogami, and H. Mori, Synth. Met. **135-136**, 665 (2003).
[20] M. Watanabe, Y. Noda, Y. Nogami, and H. Mori, J. Phys. Soc. Jpn. **73**, 116 (2004).
[21] R. Chiba, H. Yamamoto, K. Hiraki, T. Takahashi, and T. Nakamura, J. Phys. Chem. Solids **62**, 389 (2001).
[22] H. Tajima, S. Kyoden, H. Mori, and S. Tanaka, Phys. Rev. B **62**, 9378 (2000).
[23] N. L. Wang, H. Mori, S. Tanaka, J. Dong, and B. P. Clayman, J. Phys.: Condens. Matter **13**, 5463 (2001).
[24] K. Yamamoto, K. Yakushi, K. Miyagawa, K. Kanoda, and A. Kawamoto, Phys. Rev. B **65**, 085110 (2002).
[25] T. Nakamura, W. Minagawa, R. Kinami, Y. Konishi, and T. Ta-

kahashi, Synth. Met. **103**, 1898 (1999).
[26] M. Watanabe, Y. Noda, Y. Nogami, and H. Mori, J. Phys. Soc. Jpn. **76**, 124602 (2007).
[27] R. Chiba, K. Hiraki, T. Takahashi, H. M. Yamamoto, and T. Nakamura, Phys. Rev. Lett. **93**, 216405 (2004).
[28] K. Suzuki, K. Yamamoto, K. Yakushi, and A. Kawamoto, J. Phys. Soc. Jpn. **74**, 2631 (2005).
[29] K. Kanoda, K. Ohnou, M. Kodama, K. Miyagawa, T. Itou, and K. Hiraki, J. Phys. IV (France) **131**, 21 (2005).
[30] M. Kodama, M.S. thesis, University of Tokyo, 2006.
[31] Y. Nogami, J.-P. Pouget, M. Watanabe, K. Oshima, H. Mori, S. Tanaka, and T. Mori, Synth. Met. **103**, 1911 (1999).
[32] M. Watanabe, Y. Nogami, K. Oshima, H. Mori, and S. Tanaka, J. Phys. Soc. Jpn. **68**, 2654 (1999).
[33] R. Chiba, K. Hiraki, T. Takahashi, H. M. Yamamoto, and T. Nakamura, Phys. Rev. B **77**, 115113 (2008).
[34] T. Nakamura, W. Minagawa, R. Kinami, and T. Takahashi, J. Phys. Soc. Jpn. **69**, 504 (2000).
[35] F. Castet, A. Fritsch, and L. Ducasse, J. Phys. I (France) **6**, 583 (1996).
[36] A. Fortunelli and A. Painelli, Phys. Rev. B **55**, 16088 (1997).
[37] Y. Imamura, S. Ten-no, K. Yonemitsu, and Y. Tanimura, J. Chem. Phys. **111**, 5986 (1999).
[38] T. Mori, Bull. Chem. Soc. Jpn. **73**, 2243 (2000).
[39] H. Seo, J. Phys. Soc. Jpn. **69**, 805 (2000).
[40] R. H. McKenzie, J. Merino, J. B. Marston, and O. P. Sushkov, Phys. Rev. B **64**, 085109 (2001).
[41] R. T. Clay, S. Mazumdar, and D. K. Campbell, J. Phys. Soc. Jpn. **71**, 1816 (2002).
[42] J. Merino, H. Seo, and M. Ogata, Phys. Rev. B **71**, 125111 (2005).
[43] T. Mori, J. Phys. Soc. Jpn. **72**, 1469 (2003).
[44] M. Kaneko and M. Ogata, J. Phys. Soc. Jpn. **75**, 014710 (2006).
[45] H. Watanabe and M. Ogata, J. Phys. Soc. Jpn. **75**, 063702 (2006).
[46] C. Hotta and N. Furukawa, Phys. Rev. B **74**, 193107 (2006); C. Hotta, N. Furukawa, A. Nakagawa, and K. Kubo, J. Phys. Soc. Jpn. **75**, 123704 (2006).
[47] S. Nishimoto, M. Shingai, and Y. Ohta, Phys. Rev. B **78**, 035113 (2008).
[48] E. Yukawa and M. Ogata, J. Phys. Soc. Jpn. **79**, 023705 (2010).
[49] M. Udagawa and Y. Motome, Phys. Rev. Lett. **98**, 206405 (2007).
[50] Y. Tanaka and K. Yonemitsu, J. Phys. Soc. Jpn. **76**, 053708 (2007); **77**, 034708 (2008).
[51] S. Miyashita and K. Yonemitsu, Phys. Rev. B **75**, 245112 (2007).
[52] K. Kuroki, J. Phys. Soc. Jpn. **75**, 114716 (2006); Sci. Technol. Adv. Mater. **10**, 024312 (2009).
[53] B. L. Brandt, D. W. Liu, and L. G. Rubin, Rev. Sci. Instrum. **70**, 104 (1999).
[54] Y. Takahide, T. Konoike, K. Enomoto, M. Nishimura, T. Terashima, S. Uji, and H. M. Yamamoto, Phys. Rev. Lett. **96**, 136602 (2006).
[55] T. S. Inada, I. Terasaki, H. Mori, and T. Mori, Phys. Rev. B **79**, 165102 (2009).
[56] R. R. Guseinov, Phys. Status Solidi B **125**, 237 (1984).
[57] R. S. Newrock, C. J. Lobb, U. Geigenmüller, and M. Octavio, Solid State Phys. **54**, 263 (1999).
[58] V. L. Berezinskii, Sov. Phys. JETP **32**, 493 (1971); J. M. Kosterlitz and D. J. Thouless, J. Phys. C **6**, 1181 (1973).
[59] J. E. Mooij, B. J. van Wees, L. J. Geerligs, M. Peters, R. Fazio, and G. Schön, Phys. Rev. Lett. **65**, 645 (1990).
[60] R. Fazio and G. Schön, Phys. Rev. B **43**, 5307 (1991).
[61] R. Fazio and H. van der Zant, Phys. Rep. **355**, 235 (2001).
[62] J. S. Meyer, A. Kamenev, and L. I. Glazman, Phys. Rev. B **70**, 045310 (2004).
[63] T. S. Tighe, M. T. Tuominen, J. M. Hergenrother, and M. Tinkham, Phys. Rev. B **47**, 1145 (1993).
[64] P. Delsing, C. D. Chen, D. B. Haviland, Y. Harada, and T. Claeson, Phys. Rev. B **50**, 3959 (1994).
[65] A. Kanda and S.-i. Kobayashi, J. Phys. Soc. Jpn. **64**, 19 (1995).
[66] R. Yamada and S.-i. Kobayashi, J. Phys. Soc. Jpn. **64**, 360 (1995).
[67] M. V. Feigel'man, S. E. Korshunov, and A. B. Pugachev, JETP Lett. **65**, 566 (1997).
[68] E. Granato and J. M. Kosterlitz, Phys. Rev. Lett. **81**, 3888 (1998).
[69] R. Kondo, M. Higa, S. Kagoshima, H. Hoshino, T. Mori, and H. Mori, J. Phys. Soc. Jpn. **75**, 044716 (2006).
[70] J. Frenkel, Phys. Rev. **54**, 647 (1938).
[71] F. Nad, P. Monceau, and H. M. Yamamoto, J. Phys.: Condens. Matter **20**, 485211 (2008).
[72] H. F. Hess, K. DeConde, T. F. Rosenbaum, and G. A. Thomas, Phys. Rev. B **25**, 5578 (1982); M. A. Paalanen, T. F. Rosenbaum, G. A. Thomas, and R. N. Bhatt, Phys. Rev. Lett. **51**, 1896 (1983).
[73] C. Y. Chen, N. W. Preyer, P. J. Picone, M. A. Kastner, H. P. Jenssen, D. R. Gabbe, A. Cassanho, and R. J. Birgeneau, Phys. Rev. Lett. **63**, 2307 (1989).
[74] Y. Takahide, T. Konoike, K. Enomoto, M. Nishimura, T. Terashima, S. Uji, and H. M. Yamamoto, Phys. Rev. Lett. **98**, 116602 (2007).
[75] T. Mori, A. Fuse, H. Mori, and S. Tanaka, Physica C **264**, 22 (1996).
[76] S. K. Khanna, W. W. Fuller, G. Grüner, and P. M. Chaikin, Phys. Rev. B **24**, 2958 (1981), and references therein.
[77] Y. Tokura, A. Urushibara, Y. Moritomo, T. Arima, A. Asamitsu, G. Kido, and N. Furukawa, J. Phys. Soc. Jpn. **63**, 3931 (1994); Y. Tokura, Rep. Prog. Phys. **69**, 797 (2006), and references therein.
[78] A. Kurobe and H. Kamimura, J. Phys. Soc. Jpn. **51**, 1904 (1982).
[79] K. A. Matveev, L. I. Glazman, P. Clarke, D. Ephron, and M. R. Beasley, Phys. Rev. B **52**, 5289 (1995).
[80] K. Ono, D. G. Austing, Y. Tokura, and S. Tarucha, Science **297**, 1313 (2002).
[81] O. V. Lounasmaa, *Experimental Principles and Methods Below 1K* (Academic Press, London, New York, 1974), and references therein.
[82] P. J. E. M. van der Linden and K. Behnia, Rev. Sci. Instrum. **75**, 273 (2004); **75**, 2486 (2004) (erratum).
[83] G. K. White, Proc. Phys. Soc., London, Sect. A **66**, 559 (1953).
[84] S. Mercone, R. Frésard, V. Caignaert, C. Martin, D. Saurel, and C. Simon, J. Appl. Phys. **98**, 023911 (2005).
[85] D. M. Kroll, Phys. Rev. B **9**, 1669 (1974).
[86] S. Belin, K. Behnia, and A. Deluzet, Phys. Rev. Lett. **81**, 4728 (1998).
[87] M. Yamashita, N. Nakata, Y. Kasahara, T. Sasaki, N. Yoneyama, N. Kobayashi, S. Fujimoto, T. Shibauchi, and Y. Matsuda, Nat.

Phys. **5**, 44 (2009).
[88] M. Kimata, Y. Takahide, A. Harada, H. Satsukawa, K. Hazama, T. Terashima, S. Uji, T. Naito, and T. Inabe, Phys. Rev. B **80**, 085110 (2009).
[89] K. Kodama, M. Kimata, Y. Takahide, T. Terashima, H. Satsukawa, A. Harada, K. Hazama, S. Uji, K. Yamamoto, and K. Yakushi, Physica B (to be published).
[90] M. N. Baibich, J. M. Broto, A. Fert, F. Nguyen Van Dau, F. Petroff, P. Etienne, G. Creuzet, A. Friederich, and J. Chazelas, Phys. Rev. Lett. **61**, 2472 (1988).
[91] J. S. Moodera, L. R. Kinder, T. M. Wong, and R. Meservey, Phys. Rev. Lett. **74**, 3273 (1995).
[92] V. Ambegaokar and S. Teitel, Phys. Rev. B **19**, 1667 (1979).